

# Potential semiconducting high-entropy silicides based on $\text{FeSi}_2$ .

*An ab initio study with density functional  
theory and special quasi-random  
structures*

Jørn-Marcus Høylo-Rosenberg



Thesis submitted for the degree of  
Master in Materials Science for Energy and  
Nanotechnology  
60 credits

Department of Chemistry  
Faculty of mathematics and natural sciences

UNIVERSITY OF OSLO

Spring 2022



**Potential semiconducting  
high-entropy silicides based on  
 $\text{FeSi}_2$ .**

*An ab initio study with density  
functional theory and special  
quasi-random structures*

Jørn-Marcus Høylo-Rosenberg

© 2022 Jørn-Marcus Høylo-Rosenberg

Potential semiconducting high-entropy silicides based on  $\text{FeSi}_2$ .

<http://www.duo.uio.no/>

Printed: Reprosentralen, University of Oslo

# **Abstract**

# Contents

<b>1</b>	<b>Introduction</b>	<b>1</b>
<b>I</b>	<b>Theory</b>	<b>3</b>
<b>2</b>	<b>High-Entropy alloys</b>	<b>4</b>
2.1	Fundamentals . . . . .	4
2.2	Core effects and properties . . . . .	7
<b>3</b>	<b>Modeling of random alloys</b>	<b>9</b>
3.1	The Special Quasi-random Structure model . . . . .	9
3.1.1	Mathematical description . . . . .	10
3.1.2	Applications to high-entropy alloys . . . . .	12
<b>4</b>	<b>Density Functional Theory</b>	<b>16</b>
4.1	Review of Quantum Mechanics . . . . .	17
4.1.1	The Shrödinger equation . . . . .	17
4.1.2	Approximations to the many-body Shrödinger equation . . . . .	18
4.2	Kohn-Sham density functional theory . . . . .	20
4.2.1	Density functional theory . . . . .	20
4.2.2	The Kohn-Sham Equation . . . . .	21
4.3	Limitations of DFT . . . . .	22
<b>II</b>	<b>Method</b>	<b>24</b>
<b>5</b>	<b>Practical aspects of DFT</b>	<b>25</b>
5.1	The Exchange-Correlation functional . . . . .	25
5.1.1	Local density approximation . . . . .	26
5.1.2	Generalized gradient approximation . . . . .	26
5.1.3	Meta-GGA . . . . .	26
5.1.4	Hybrid functionals . . . . .	27
5.1.5	Outlook . . . . .	28
5.2	Plane waves and reciprocal space . . . . .	28
5.3	Self-consistent field calculation . . . . .	31

<b>6</b>	<b>Computational details</b>	<b>32</b>
6.1	Settings and dependencies . . . . .	32
6.2	Material . . . . .	33
<b>III</b>	<b>Results and Discussion</b>	<b>35</b>
<b>7</b>	<b>The high-entropy silicide (CrFeMnNi)Si<sub>2</sub></b>	<b>36</b>
7.1	Bulk $\beta$ -FeSi <sub>2</sub> . . . . .	36
7.2	(CrFeMnNi)Si <sub>2</sub> SQSs . . . . .	37
7.2.1	The band gap . . . . .	39
7.2.2	Local and projected density of states . . . . .	43
7.2.3	The band gap with SCAN and HSE06 . . . . .	45
7.2.4	Pair distribution functions . . . . .	50
7.2.5	Charge density . . . . .	51
7.2.6	SQS size . . . . .	52
<b>8</b>	<b>Alternative compositions</b>	<b>56</b>
8.1	Exploring the quaternary phase diagram . . . . .	56
8.2	High entropy silicides with cobalt/titanium . . . . .	60
<b>IV</b>	<b>Conclusion and future work</b>	<b>65</b>
<b>9</b>	<b>Conclusion</b>	<b>66</b>
<b>10</b>	<b>Future work</b>	<b>68</b>
<b>A</b>	<b>Figures</b>	<b>69</b>
A.1	Density of states . . . . .	69
A.2	Projected density of states . . . . .	71
A.3	Charge density . . . . .	72
A.4	Other . . . . .	73

# List of Figures

2.1	Formation of HEA based on $\delta$ and $N$ . Figures adopted from [hea2016_ch2] . . . . .	6
2.2	A schematic illustration of lattice distortion in high-entropy alloys. Figure from [owen_jones_2018] . . . . .	8
3.1	PDFs of (a) 20 and (b) 250 atom SQS models of CrFeMnNi [hea2016_ch10] . . . . .	13
3.2	Density of states with SQS and MC/MD of FCC CoCrFeNi, figure from [hea2016_ch10] . . . . .	14
3.3	Probability distribution functions with SQS and MC/MD of HCP CoOsReRu [hea2016_ch10] . . . . .	14
4.1	Number of DFT studies per year from 1980 to 2021 [dimensions]. . . . .	16
5.1	Jacob's ladder [jacob]. . . . .	25
5.2	Calculated to experimental band gap measurements of Becke-Johnson, modified Becke-Johnson and SCAN functionals [xc_benchmark] . . . . .	27
5.3	Self consistent iterations of a DFT calculation. Figure adopted from the lecture notes in FYS-MENA4111 [persson2020] . . . . .	31
6.1	Five distinct 48-atom SQSs of $\text{Cr}_4\text{Fe}_4\text{Mn}_4\text{Ni}_4\text{Si}_{32}$ based on the $\beta$ -FeSi <sub>2</sub> crystal structure. Manganese atoms are represented as purple spheres, chromium as dark blue and silicon as light blue, followed by iron and nickel presented as gold and silver spheres respectively. The respective SQSs are denoted as A, B, C, D and E. Figures illustrated with VESTA [vesta] . . . . .	34
7.1	Density of states (PBE) $\beta$ -FeSi <sub>2</sub> . . . . .	37
7.2	Density of states of SQS D (CrFeMnNi)Si <sub>2</sub> with PBE. . . . .	39
7.3	Density of states of SQS B (CrFeMnNi)Si <sub>2</sub> with PBE. . . . .	39
7.4	Local density of states of Si (SQS D) . . . . .	43
7.5	Local density of states of (a) Cr, (b) Mn, (c) Fe, (d) Ni in SQS D. . . . .	43
7.6	Projected density of states SQS D CFMN (fesi2) from PBE calculation . . . . .	44
7.7	Projected density of states of SQS D and B around $E_F$ . . . . .	44
7.8	Density of states illustrating the band gaps from PBE and SCAN calculations for SQS E and D. . . . .	46



7.9	Density of states of SQS B with HSE06 . . . . .	46
7.10	Pair distribution functions of SQS D (top) and B (bottom) . .	50
7.11	Charge density in SQS A, B, D and E of $\text{Cr}_4\text{Fe}_4\text{Mn}_4\text{Ni}_4\text{Si}_{32}$ . .	51
7.12	CPU time of 48, 96 and 192-atom SQSs of $(\text{CrFeMnNi})\text{Si}_2$ . .	52
7.13	Density of states of SQS E 192 atom SQS. . . . .	54
7.14	Pair distribution functions of $(\text{CrFeMnNi})\text{Si}_2$ (top) 48-atom SQS, (middle) 96-atom SQS, (bottom) 192-atom SQS. . . . .	55
8.1	Projected density of states of (a) $\text{Cr}_3\text{Fe}_3\text{Mn}_7\text{Ni}_3\text{Si}_{32}$ (SQS B), (b) $\text{Cr}_5\text{Fe}_5\text{Mn}_3\text{Ni}_3\text{Si}_{32}$ (SQS C), (c) $\text{Cr}_5\text{Fe}_3\text{Mn}_5\text{Ni}_3\text{Si}_{32}$ (SQS A), (d) $\text{Cr}_3\text{Fe}_5\text{Mn}_5\text{Ni}_3\text{Si}_{32}$ (SQS D) . . . . .	58
8.2	Projected density of states of $\text{Cr}_3\text{Fe}_3\text{Mn}_3\text{Ni}_7\text{Si}_{32}$ around $E_F$ .	59
8.3	Projected density of states of $(\text{CrFeMnCo})\text{Si}_2$ . . . . .	63
8.4	Projected density of states . . . . .	63
8.5	Density of states of two SQS A and E of $(\text{CoFeMnNi})\text{Si}_2$ . . .	64
A.1	Density of states SQS A $(\text{CrFeMnNi})\text{Si}_2$ with PBE. . . . .	69
A.2	Density of states SQS E $(\text{CrFeMnNi})\text{Si}_2$ with PBE. . . . .	70
A.3	Density of states SQS C $(\text{CrFeMnNi})\text{Si}_2$ with PBE. Nedos represent the number of points in the DOS calculation. . . .	70
A.4	Projected density of states SQS A . . . . .	71
A.5	Projected density of states SQS B . . . . .	71
A.6	Projected density of states SQS E . . . . .	72
A.7	Charge density of SQS C. . . . .	72
A.8	Density of states SQS C $\text{Cr}_5\text{Fe}_5\text{Mn}_3\text{Ni}_3\text{Si}_{32}$ , illustrating the small finite DOS at $E_F$ due to the impurity gap. . . . .	73

# List of Tables

7.1	Total energy per atom, final magnetic moment and band gap of 5 unique SQS of (CrFeMnNi)Si <sub>2</sub> based on the $\beta$ -FeSi <sub>2</sub> unit cell. . . . .	37
7.2	Band gap of the 5 SQSs of (CrFeMnNi)Si <sub>2</sub> calculated from the eigenvalues in spin up, down and total. . . . .	40
7.3	Band gap of SQS D as a function of occupancy in the eigenvalues. . . . .	41
7.4	Band gap calculated with PBE, SCAN and HSE06 XC-functionals of (CrFeMnNi)Si <sub>2</sub> SQSs. . . . .	45
7.5	Minimum gap between k-point in valence band and conduction band in SQS B from PBE, SCAN and HSE06 . . . . .	47
7.6	Band gap from HSE06 calculations with Gaussian smearing and smearing width <i>sigma</i> equal to 0.05 and 0.005, and the tetrahedron method (TBC). "-" means unchanged . . . . .	48
7.7	Total energy, magnetic moment and formation energy of 48, 96 and 192 atom SQSs of (CrFeMnNi)Si <sub>2</sub> . . . . .	52
7.8	Band gap of SQSs of 48, 96 and 192-atoms of (CrFeMnNi)Si <sub>2</sub> . The names are arbitrary, ie A in 48 does not equal A in 96 or A in 192. The values listed in <i>cursive</i> indicate a defect band gap. . . . .	53
8.1	Summary composition diagram . . . . .	56
8.2	Band gaps of various compositions of (CrFeMnNi)Si <sub>2</sub> . Most stable SQS of a set is highlighted in bold text, defect/impurity band gap are listed in cursive. Some SQSs were excluded from the table due to unsuccessful calculations. . . . .	57
8.3	Overview new compositions . . . . .	60
8.4	Final magnetic moment of the utmost stable SQS of each composition. . . . .	61
8.5	The band gap in spin up/down and total of the utmost stable SQS in five high-entropy silicides based on $\beta$ -FeSi <sub>2</sub> . . . . .	62

# Acknowledgments

I would like to express my gratitude towards my supervisor Ole Martin Løvvik. For always being available and prioritize my work from the first day to the last. Coming into this project, I had no prior knowledge of density functional theory or quantum mechanical modeling. So, for your guidance in this project I am truly thankful, and know that this project would have been impossible without you. I also feel as if I have made a friend and someone I could talk through throughout this project. Due to the oddity of these recent years with the covid-19 outbreak and self-isolation this have been very important to my sanity and mental health combined with the difficulty involved in writing a master theses. On this same note, I would like to thank all my friends and family members that have been there and believed in me, and always reminding me to stay positive.

# Chapter 1

## Introduction

A major concern in the energy sector is the loss of energy as waste heat. For instance [1] point to as of 2012 in USA that about 60% is lost in the process. Thermoelectricity as opposed to energy sources such as solar power that generate waste heat, can generate electricity from heat by what's known as the Seebeck effect [2]. However, thermoelectricity is today limited to niche markets because of low efficiency. This can be explained from the thermoelectric figure of merit composed of the seebeck Coefficient  $S$ , electrical conductivity  $\sigma$ , temperature  $T$  and the thermal conductivity, in the following relation [3]

$$zT = \frac{S^2\sigma T}{\kappa}. \quad (1.1)$$

Thus, to design a efficient thermoelectric material one needs to optimize three dependent variables: High Seebeck coefficient, high electrical conductivity, and low thermal conductivity. A popular strategy is the phonon-glass electron crystal approach [4], in which one will introduce complexity and aharmonicity to the crystal lattice by some means to increase levels of phonon scattering to reduce the thermal conductivity, without affecting the electrical conductivity of the material. Furthermore good thermoelectrics are generally considered narrow gap semiconductors [5], preferably between  $6-10 k_B T$ , which at room temperature makes out to around 0.2 eV.

In this project we will look at high-entropy alloys as potential thermoelectric materials. High-entropy alloys are a novel material class that extends the concept of traditional binary-alloys such as steel, to multi-component alloys. The name "high-entropy" stems from the fact that mixing a larger number of elements increase the configurational entropy of the solution, and helps stabilize the materials. These types of materials are in particular known for their strong mechanical properties [6], for instance high strength at elevated temperatures and indication of that the disordered structure caused by different elements in the lattice, causes increased levels of phonon scattering, without similar effects to electron scattering. Hence, provided that one can find narrow gap high-entropy alloys, these could be relevant as thermoelectrics due to the an-harmonic structure and high-temperature stability most notably.

Specifically, in this project we will look at high-entropy silicides. These are a lesser known and studied subclass of high-entropy alloys, the first experimentally synthesized high-entropy silicide was found in 2019 by Gild. et al [7]. Discovering a first of its kind single-phase high-entropy disilicide  $(\text{MoNbTaW})\text{Si}_2$ . This silicide adopted the hexagonal C40 crystal structure, and displayed low thermal conductivity compared to conventional disilicides in the equivalent crystal structure. Additionally, very recently a master thesis student at the University of Oslo managed to synthesize three phases of non-cubic high-entropy silicides based on Si, Co, Cr, Fe, and Ni in both hexagonal and orthorhombic symmetries [8]. We base this project on silicides because firstly silicon and various transition metal-silicides are environmentally sound and silicon in particular is heavily applied in micro-electronic devices and renewable energy sources such as solar power, thus silicon based alloys could readily be implemented into these technologies. Secondly, transition metal silicides offer a good range of initial compounds with suitable band gaps for thermoelectrics [9]. Hence, these emerge as a natural initial selection for our purpose.

Here, we perform an ab initio study utilizing the special quasi-random structures method in combination with density functional theory to perform numerical simulations of potential high-entropy silicides. The materials in this project are based on the semiconductor  $\beta\text{-FeSi}_2$ , here-in just  $\text{FeSi}_2$ , where we populate the iron sites in the structure by numerous configurations of a combination of 3d transition metals. The main objective of this thesis is to locate semiconductors, thus the majority of this project will revolve around studying the band gap of the various materials. We begin this project by reviewing the fundamentals and properties of high-entropy alloys, thereafter we present a theoretical description of the computational methods in this project, SQS, and DFT. Next we discuss various practical aspects of DFT such as the exchange-correlation functionals and numerical convergence, in addition to numerical settings necessary to reproduce the results in this project. Finally we present and discuss the results, which begin with the high-entropy silicide  $(\text{CrFeMnNi})\text{Si}_2$ , followed by various derivatives and alternatives to this system. In the end we give a brief conclusion of our work and summarize our findings and outline possible directions for future research.

# **Part I**

# **Theory**

# **Part II**

## **Method**

**Part III**

**Results and Discussion**



## Chapter 7

# The high-entropy silicide (CrFeMnNi)Si<sub>2</sub>

### 7.1 Bulk $\beta$ -FeSi<sub>2</sub>

We begin by presenting a brief overview of the parent compound  $\beta$ -FeSi<sub>2</sub> that we have used as a foundation in this project.. In addition this is the sole case in this project where our methods and results can be compared to experimental work and relevant literature.

$\beta$ -FeSi<sub>2</sub> is a well known semiconductor with an experimentally measured band gap of around 0.85 eV at room temperature [10]. The nature of the band gap is under debate, all though most ab initio studies result in an indirect gap, experimental studies agree on a direct band gap. From our own calculations we get an indirect band gap of 0.65 eV with PBE GGA functional. In comparison materials project list a band gap of 0.70 eV with the same functional. This slight discrepancy is most likely down to use of different parameters in the calculations, for example the cutoff energy or number of k-points. In agreement with materials project our calculations return a final magnetic moment of the compound equal to 0, this can be seen in the electronic density of states of the material plotted in figure 7.1, by that the DOS and hence band gap is identical in both spins.

The formation energy  $E_{\text{form}}$  of the compound can be calculated as the difference in total energy between the product and the sum of reactants. For the FeSi<sub>2</sub> compound that consist of 16 iron atoms and 32 silicon we get

$$E_{\text{form}} = -327.72\text{eV} - (16 \times -8.32\text{eV} + 32 \times -5.42\text{eV}) = -21.16\text{eV},$$

or formation energy per atom  $E_{\text{FPA}} = 0.441\text{eV}$  from  $-21.16/48$ . The total energy of iron and silicon was calculated separately for the respective base elements with identical parameters as used for the FeSi<sub>2</sub> calculation. The total energies correspond well with the listed energies from materials project of -8.4693 eV and -5.4234 eV for Fe and Si respectively. Accordingly the formation energy per atom for  $\beta$ -FeSi<sub>2</sub> of 0.441 eV is in good agreement with materials project's value of 0.444 eV for  $\beta$ -. Again, the

difference is most likely related to materials project utilizing a larger energy cutoff of 520 eV compared to our value of 300 eV.

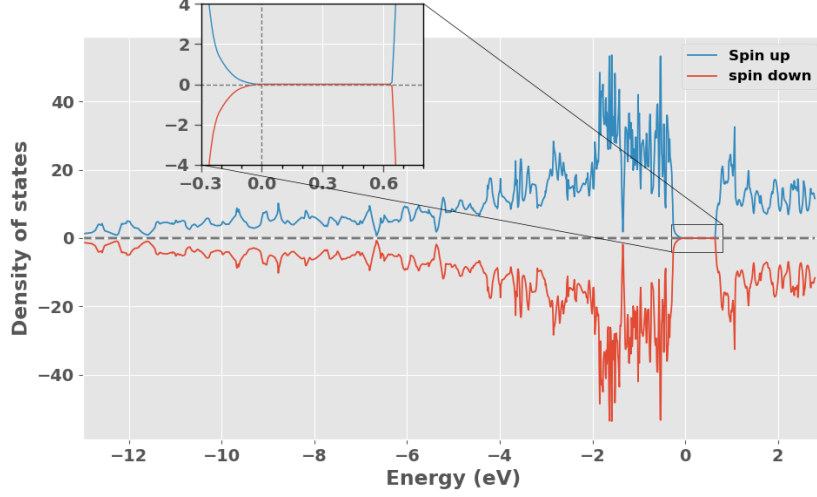


Figure 7.1: Density of states (PBE)  $\beta$ -FeSi<sub>2</sub>

## 7.2 (CrFeMnNi)Si<sub>2</sub> SQSs

Below in table 7.1 we list the total energy per atom (Toten), final magnetic moment per atom (Mag) and band gap ( $E_G$ ) of five unique SQSs of the Cr<sub>4</sub>Fe<sub>4</sub>Mn<sub>4</sub>Ni<sub>4</sub>Si<sub>32</sub> alloys based on the  $\beta$ -FeSi<sub>2</sub> structure. In addition we include the mean and standard deviation (std) between the 5 supercells and the formation energy calculated from the mean total energy. Details on the generation and general features of the SQSs are provided in section 6.2.

SQS	Toten (eV)	Mag ( $\mu_B$ )	$E_G$ (eV)
A	-6,6080	0.0833	0.0280
B	-6,6138	0.0833	0.0523
C	-6,6063	0.0834	0.0344
D	-6,6155	0.0833	0
E	-6,6089	0.0833	0.0495
Mean	-6.6105	0.0833	0.0328
Std	0.0039	0.0000	0.0210
$E_{FPA}(eV)$	-0.293	-	-

Table 7.1: Total energy per atom, final magnetic moment and band gap of 5 unique SQS of (CrFeMnNi)Si<sub>2</sub> based on the  $\beta$ -FeSi<sub>2</sub> unit cell.

From table 7.1 we observe that the total energy and magnetic moment are quite similar in all 5 supercells, which could be expected from that the atomic configuration is the only variable. On the other hand the atomic

configuration have a larger impact on the band gap of the supercells. We find that the band gap ranges from a maximum value of 0.05 eV in SQS B, to a metal in SQS D, nevertheless much smaller than FeSi<sub>2</sub> (0.65 eV). We will come back to discussing the band gaps in later sections.

Compared to the bulk material we find that the alloy apparent from all five supercells display a finite magnetic moment of around  $0.083\mu_B$ . The local magnetic moments show some variation between supercells but follow the same trend where the largest moments are attributed to chromium atoms in the lattice, followed by manganese. On the other side the magnetic moments of both iron and nickel within the numerical accuracy of the calculations give negligible contributions to the magnetic moment of the structures. Considering that the total magnetic moment is identical in 5 distinct atomic configurations and the local magnetic moments show very similar trends, the observed magnetism within the scope of this project is most probably connected to the particular crystal structure. It should be noted however that the magnetic properties in this project could be prone to errors. As we discussed in section 4.3 one of the major drawbacks of DFT in regards to magnetic materials is the local minima problem. In this project we have overlooked this concern and applied a constant initial co-linear magnetic configuration in all structures in order to reduce the workload, thus it's possible that the final magnetic structure of the supercells adopt local minimas rather than global. Coupling this with the possible errors associated with the special quasi-random structures method to model the disordered magnetic structure means that the magnetic results and following the total energy and corresponding stability are not immutable nor necessarily accurate in respect to the hypothetical real alloy.

In terms of the total energy the most and least stable SQSs are "D" and "A" respectively, meaning that SQS D is then the most representative configuration of the real material. However most likely all five SQSs and other possible configurations would appear as local orderings in domains of the real material with a certain probability. Therefore we will consider and discuss the results of all 5 SQSs as well as the most stable supercell. Further the total energy alone is not sufficient to evaluate the stability of the structure. In this project we have not considered factors such as the configurational entropy or made any finite temperature considerations in general. Additionally the discussion above on the magnetic configuration could affect the total energy. Thus the relative stability between supercells listed in table 7.1 could be variable, nevertheless the most stable configuration is moderately emphasized from the considerations made in this project.

### 7.2.1 The band gap

As seen from table 7.1 the band gap of the alloy are severely reduced from the bulk material, and vary from supercell to supercell. We observed a maximum band gap of 0.05 eV in SQS B, and on the flip side a 0 band gap in the utmost stable configuration SQS D. The density of states of SQS D and B is displayed in figures 7.2 and 7.3 below, similar plots can be found in appendix A.1 of the other SQSs.

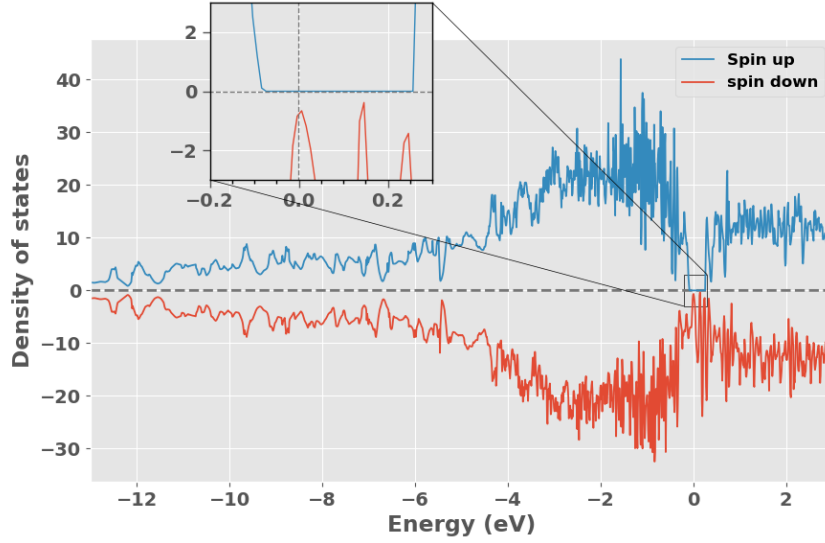


Figure 7.2: Density of states of SQS D (CrFeMnNi)Si<sub>2</sub> with PBE.

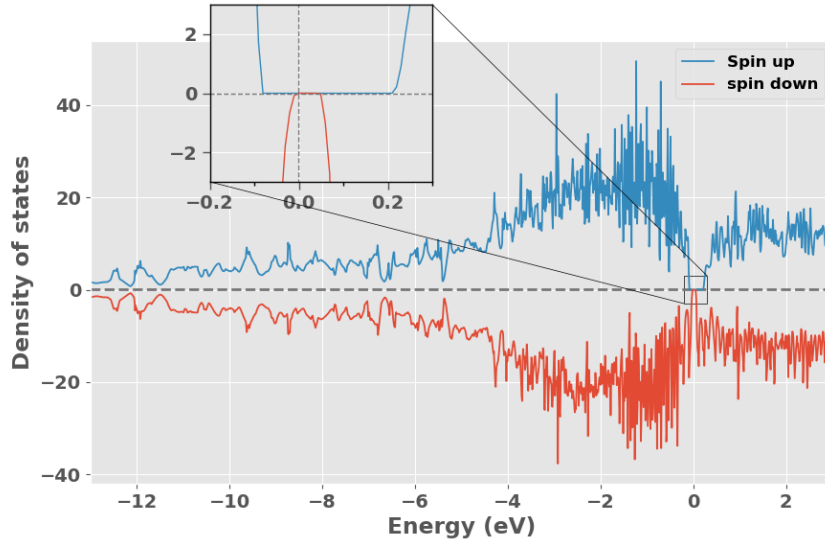


Figure 7.3: Density of states of SQS B (CrFeMnNi)Si<sub>2</sub> with PBE.

In figure 7.2 and 7.3 we observe that the band gap in both SQS D and B

in accordance with the magnetic property is different between spins. Going forward we will refer to the band gap in spin up as  $E_G^{\text{up}}$ , and spin down as  $E_G^{\text{dw}}$ . Clearly in both D and B  $E_G^{\text{up}} \gg E_G^{\text{dw}}$  as SQS D for instance exhibits a band gap of around 0.3 eV in spin up, contrary to a 0 band gap in spin down. Comparing to the values in table 7.1 we find that the total band gaps of the respective structures is limited by the narrow or nonexistent band gap in spin down. To obtain further and more precise information on the band gap we look to the calculated Kohn-Sham eigenvalues. The eigenvalue band gaps, denoted as  $E_G^{\text{eigen}}$  can be seen below in table 7.2 for all five SQS, where the utmost stable configuration (SQS D) is highlighted in bold text. Continuing the trend described above we observe equivalent to SQS D and B that  $E_G^{\text{up}} \gg E_G^{\text{dw}}$  for all supercells, par SQS A where the spin polarization of the band gap is less prominent and the total band gap is the combined sum of  $E_G^{\text{up}}$  and  $E_G^{\text{dw}}$ .

SQS	$E_G^{\text{up, eigen}}$ (meV)	$E_G^{\text{dw, eigen}}$ (meV)	$E_G^{\text{tot, eigen}}$ (meV)
A	81.4	52.2	28.1
B	293	52.2	52.2
C	236	34.3	34.3
<b>D</b>	339	0.00	0.00
E	308	50.0	50.0

Table 7.2: Band gap of the 5 SQSs of (CrFeMnNi)Si<sub>2</sub> calculated from the eigenvalues in spin up, down and total.

In VASP the energy eigenvalues are listed for every energy band at all k-points used in the calculation, with corresponding occupancy. An occupancy of 1 represents a fully occupied eigenstate, in analog a completely unoccupied (empty) eigenstate have occupancy equal to 0. Recalling that occupied states belong to the valence band, and the conduction band consists of unoccupied states (at 0 K). The highest energy valence band in these structures are band 124 in spin down and 128 in spin up, following the lowest energy valence band is 125/129 in spin down/up. The band gap in spin down is then determined from the difference between the lowest energy eigenvalue in band 125 and the highest energy eigenvalue in band 124, and likewise for the spin up band gap between bands 128 and 129. In SQS D different from the semiconducting structures we observe some partially occupied states at the band edges in bands 124 and 125 in spin down. With partially occupied states we refer to eigenstates in the valence band with occupancy less than 1 and states in the conduction band with occupancy above 0. Specifically the highest energy eigenvalue (9.01 eV) in band 124 have occupancy equal to 0.94, and equivalently the lowest energy eigenvalue (8.98 eV) in band 125 have occupancy equal to 0.08. This results in a 0 (negative) band gap. Further the Fermi energy in this structure is 8.99 eV, the partially occupied eigenstate in band 124 is then above the Fermi energy, and the partially unoccupied eigenstate in

the conduction band below the Fermi energy. This is a clear indication of a metal, in which the conduction band and valence band overlap. In this project we will refer to such eigenstates with partial occupancy as defect states. The importance of the defect states on the band gap in SQS D can be seen clearly in table 7.3. Here we calculate the band gap as a function of the defect states by an occupancy parameter  $occ$ , such that  $E_G(0.99, 0.01)$  is the band gap when only including eigenvalues with corresponding occupancy above 0.99 in the valence band and below 0.01 in the conduction band. For simplicity we will write the parameter as a single value, where  $occ = 0.01$  represents occupancy equal to 1 - 0.01 in the valence band and 0 + 0.01 in the conduction band.

$occ$	$E_G^{\text{up, eigen}}$ (meV)	$E_G^{\text{dw, eigen}}$ (meV)	$E_G^{\text{tot, eigen}}$ (meV)
0.5	339	0	0
0.05	339	21.0	21.0
0.01	339	49.6	49.6
0.001	339	73.3	73.3
<0.0001	339	85.7	85.7

Table 7.3: Band gap of SQS D as a function of occupancy in the eigenvalues.

From table 7.3 we find clear evidence of the defect states prohibiting the band gap in spin down in SQS D, compared to the semiconducting supercells that contain only fully occupied and unoccupied eigenstates. To investigate this effect to greater extent we compare the eigenvalues of SQS D to a pure metal, such as iron. In this case the energy bands (both spins) around the Fermi energy (5.8 eV) is populated mostly by partially filled eigenstates. Inside a single energy band we observe instances of both more than half-filled states above  $E_F$ , and less than half-filled states above  $E_F$ , thus clearly overlap between the conduction and valence band. In contrast we find no instances of partial occupants in pure Si, as in the semiconducting SQSs. Therefore we can firmly state that the "defect states" are associated with a metallic character. Compared to the pure metal however, the amount and severity of the partial occupants are very dampened in SQS D. The concept of defect or impurity states in the band gap have been found as a common feature of the band structure of random alloys [11], however we have reservations about if this is a physical result or related to numerical factors. In addition to partial occupants in Fe and SQS D we observe a plural of non-naturalistic states where the occupancy exceeds 1 and 0. Recalling that the discontinues Fermi surface of metals poses several obstacles on DFT calculations with respect to the smearing and number of k-points. This result could then be imagined as a consequence of numerical methods. For instance in SQS B we conducted three separate electronic calculations, one with the tetrahedron method (value listed in tables) and two calculations with Gaussian smearing with smearing width 0.05 and 0.005 eV. With the Gaussian method and smearing

width  $\sigma = 0.05\text{eV}$  we get  $E_G^{\text{up, eigen}} = 0.2987\text{eV}$  and  $E_G^{\text{dw, eigen}} = 0.0497\text{eV}$ . Further calculations with the Gaussian method with smearing width of  $0.005\text{ eV}$  results in  $E_G^{\text{up, eigen}} = 0.2932\text{eV}$  and  $E_G^{\text{dw, eigen}} = 0.0522\text{eV}$ . Compared to the values in table 7.3 with TBC, we observe that Gaussian ( $0.005\text{ eV}$ ) and TBC are identical, while Gaussian ( $0.05\text{ eV}$ ) show some deviation. Furthermore we find that the eigenvalues of Gaussian  $0.05\text{ eV}$  contain defect states, and that the spin down band gap can thus be enlarged as in SQS D previously by  $E_G^{\text{dw, eigen}}(0.01) = 0.1695\text{eV}$ . However, in this case we find no instances of non-naturalistic states as we described above for SQS D with TBC.

In conclusion, the defect states observed in SQS D is clearly related to a metallic structure, however from the discussion above we have seen that the results could be subject to numerical factors as well. It would have been instructive to visualize and analyze the eigenvalues by plotting the band structure. Unfortunately this is neither simple to perform or interpret for large supercells consisting of several elements and a large number of energy bands. One solution could be band-unfolding, but this did not work in conjunction with the implementation of the SQS method in this project.

### 7.2.2 Local and projected density of states

In this section we will analyze the local and projected density of states of primarily SQS D (most stable). Below we include the local density of states of silicon in figure 7.4, and the respective LDOS plots of the various 3d elements of the compound in figure 7.5.

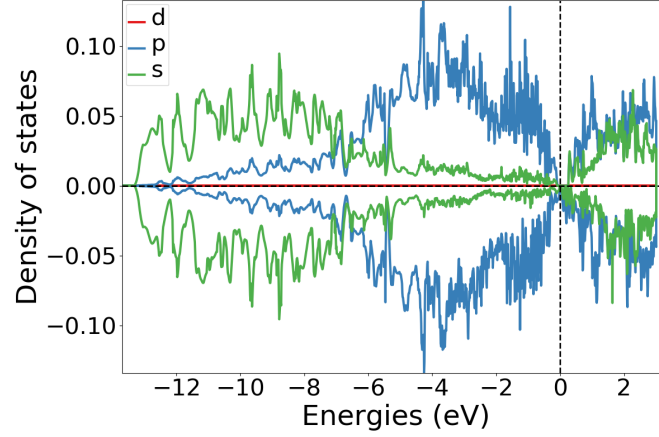


Figure 7.4: Local density of states of Si (SQS D)

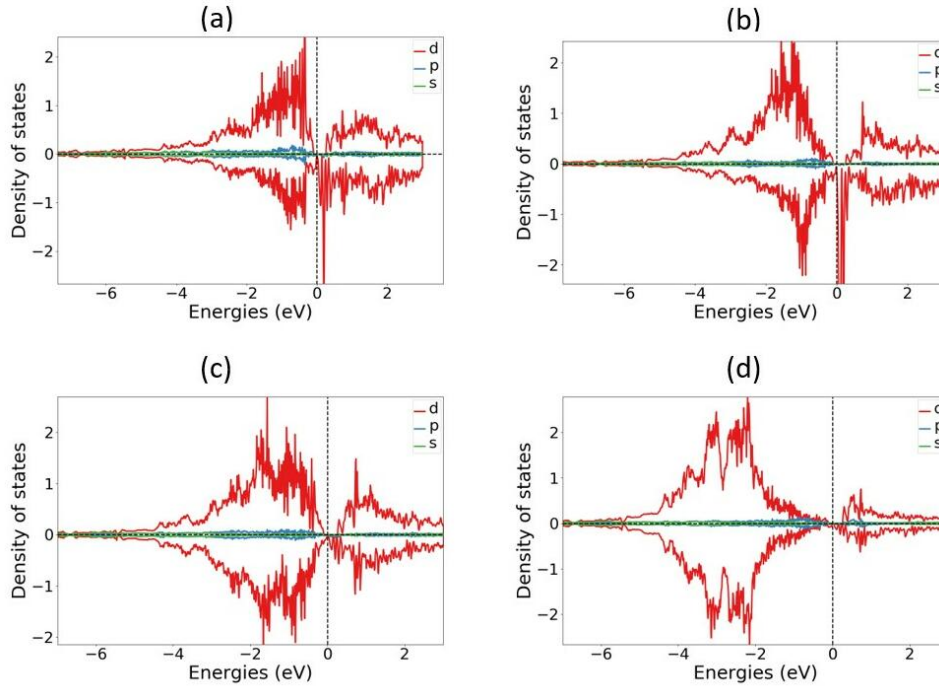


Figure 7.5: Local density of states of (a) Cr, (b) Mn, (c) Fe, (d) Ni in SQS D.

In the local density of states plotted in figure 7.4 we see that the s-electrons in Si occupy states in the lower energy regions and p electrons at slightly elevated energies closer to the Fermi energy. Above  $E_F$  states



are occupied by s and p electrons equally. Between the 3d electrons of the transition metals, markedly manganese and chromium display a strong presence at energies just above  $E_F$  and manganese additionally below  $E_F$ . Iron and Nickel show largest contributions at energies further from the Fermi energy, most notably below  $E_F$ . In the spin up channel we see a similar trend where chromium lies closest to  $E_F$  followed by manganese, iron and lastly nickel at the lowest energies. It could also be noted that in relation to the local magnetic moments discussed previously, we observe that the local density of states is symmetric with respect to spin in Fe and Ni, but not in Cr and Mn.

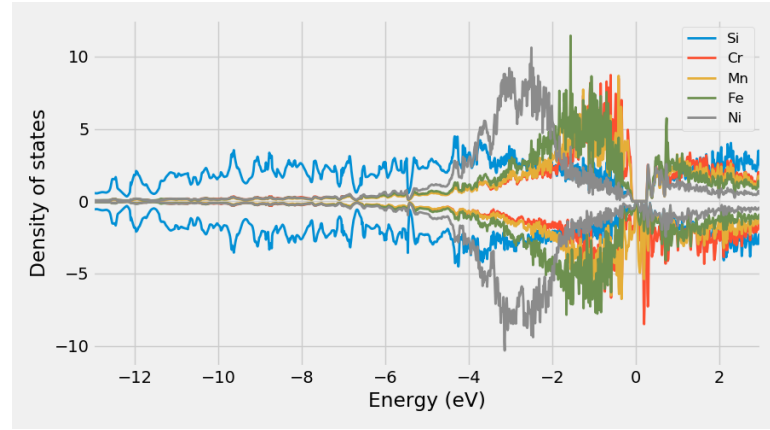


Figure 7.6: Projected density of states SQS D CFMN (fesi2) from PBE calculation

The interplay between 3d elements and silicon as shown in the projected density of states (figure 7.6) is in good agreement with observed trends in simpler Si-rich transition metal silicides [12] and Fe and Si  $\beta$ -FeSi<sub>2</sub> [13].

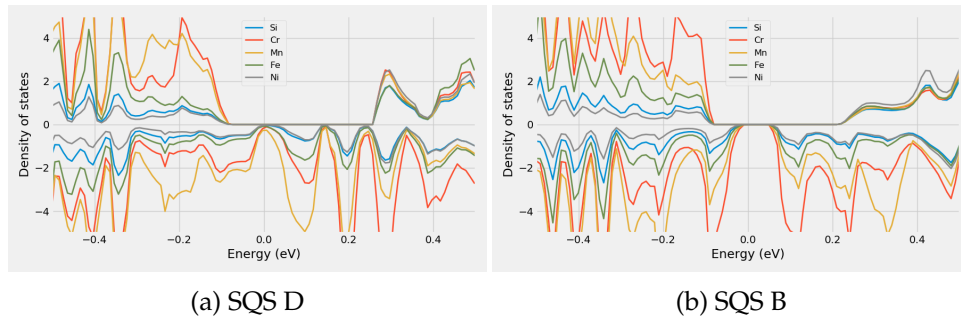


Figure 7.7: Projected density of states of SQS D and B around  $E_F$

Comparing the PDOS of half-metallic SQS D (figure 7.7 a) to the configuration with the largest  $E_G^{\text{dw}}$  SQS B (figure 7.7 b), we find distinctly a large number of Mn states in SQS D around  $E_F$  most noticeably in spin down, but also in spin up. The PDOSs of SQSs A, B, and E are included in appendix A.2 (unable to plot PDOS for SQS C)

### 7.2.3 The band gap with SCAN and HSE06

As expressed previously, in this work we invoke 3 level of depths GGA (PBE), meta-GGA (SCAN) and hybrid functional (HSE06) to determine the band gap. The outcome of these 3 functionals are showcased in table 7.4.

SQS	XC-functional	$E_G^{\text{up}}$ (eV)	$E_G^{\text{dw}}$ (eV)	$E_G^{\text{tot}}$ (eV)
A	PBE	0.0815	0.0521	0.0281
	SCAN	0	0	0
	HSE06	0.7084	0.0261	0.0261
B	PBE	0.2932	0.0523	0.0523
	SCAN	0.1470	0.0890	0.0890
	HSE06	0.2855	0.1819	0.1819
C	PBE	0.2355	0.0343	0.0343
	SCAN	0.0690	0.1124	0.1124
	HSE06	0.1744	0.0328	0.0196
D	PBE	0.3386	0	0
	SCAN	0	0.1086	0
	HSE06	0.3780	0	0
E	PBE	0.3078	0.0495	0.0495
	SCAN	0.1540	0.1112	0.1048
	HSE06	0.5476	0.0133	0.0133

Table 7.4: Band gap calculated with PBE, SCAN and HSE06 XC-functionals of (CrFeMnNi)Si<sub>2</sub> SQSs.

We will begin dissecting table 7.4 by comparing SCAN to PBE. The first distinction we make notice of is in SQS A. In this supercell calculations with the SCAN functional predicts a metallic compound, contrary to the the PBE band gap of 0.03 eV. Alike the band gap of SQS D discussed previously, the 0 band gap in this structure with SCAN is caused by defect states. Neglecting such states and evaluating the band gap from just completely filled and empty eigenstates yield  $E_{G,\text{SCAN}}^{\text{up,eigen}}(0.99,0.01) = 0.0316$  eV and  $E_{G,\text{SCAN}}^{\text{dw,eigen}}(0.99,0.01) = 0.0531$  eV, and a total band gap of 0.0316 eV. This value seems to agree better with the PBE band gap of this supercell, but we observe that  $E_G^{\text{up}}$  is larger in PBE. This is a recurrent patter with SCAN across all five SQSs, where  $E_{G,\text{SCAN}}^{\text{up}} < E_{G,\text{PBE}}^{\text{up}}$ , and moreover  $E_{G,\text{SCAN}}^{\text{dw}} > E_{G,\text{PBE}}^{\text{dw}}$ . This can be seen in figure 7.8, where we plot the density of states of SQS E (a, b) and C (c, d). Note that the SCAN band gap in SQS C have the opposite spin polarization of PBE, this is also the case in SQS D as seen from table 7.4.

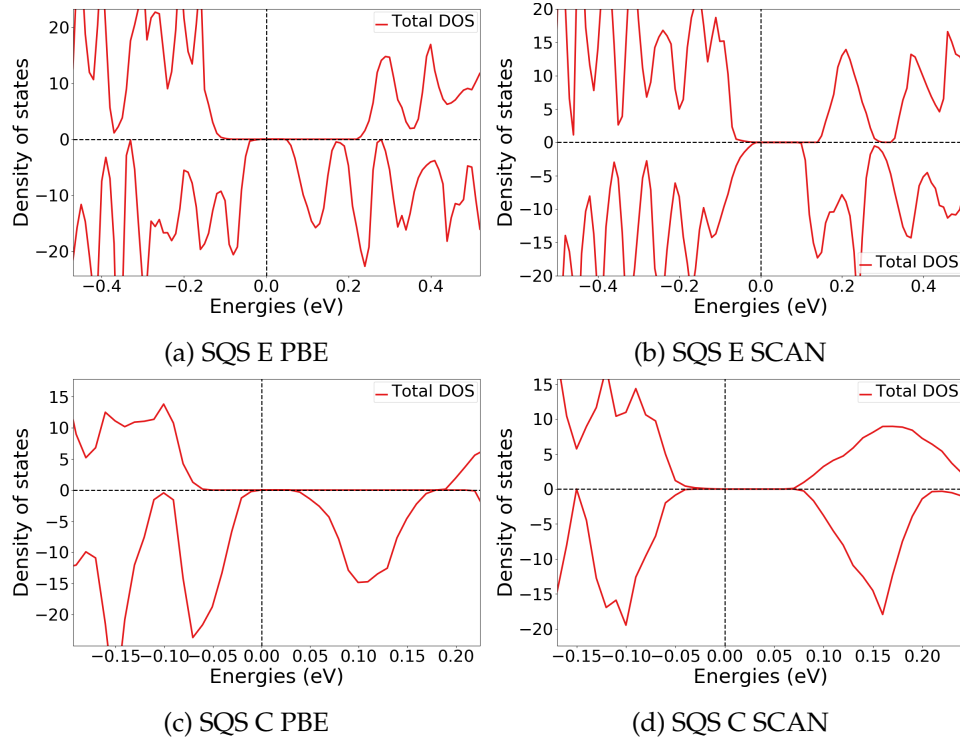


Figure 7.8: Density of states illustrating the band gaps from PBE and SCAN calculations for SQS E and D.

With the HSE06 functional we observe the opposite trend to SCAN in SQS A and E, where  $E_{G, \text{HSE06}}^{\text{up}} > E_{G, \text{PBE}}^{\text{up}}$  and  $E_{G, \text{HSE06}}^{\text{dw}} < E_{G, \text{PBE}}^{\text{dw}}$ . But in other cases  $E_{G, \text{HSE06}}^{\text{up}}$  is lesser (SQS C) or similar to PBE (SQS B and D). On the other hand  $E_{G, \text{HSE06}}^{\text{dw}}$  is consistently smaller in all structures compared to PBE, with the exception of SQS B. In this structure the HSE06 functional predicts large band gaps in both spins, as seen from the density of states plotted in figure 7.8.

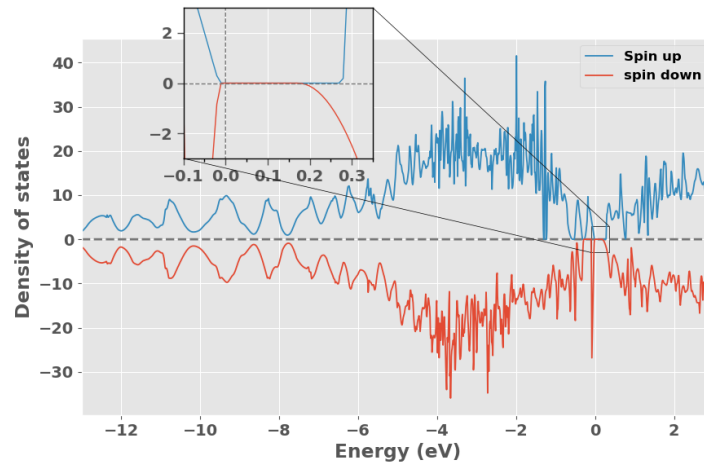


Figure 7.9: Density of states of SQS B with HSE06

As we discussed in section 5.1, hybrid functionals are much more computationally demanding compared to both meta-GGA and GGA functionals. In this project we experienced particular difficulty of converging calculations with HSE06 of the compositionally complex structures. To reduce the cost of the HSE06 functional we performed such calculations with a lower density of k-points, see section 6.1. The small amount of k-points could as discussed lead to numerical inaccuracies relating to the calculation of the Fermi surface in metallic structures. Furthermore the reduced mesh of k-points could result in artificially exaggerated band gaps from failing to encapsulate the exact minimum transition between the valence band and conduction band.

XC-functional	Transition (k-point)
PBE	(0.250,0.000,0.250) $\rightarrow$ (0.000,0.000,0.000)
SCAN	(0.250,0.000,0.250) $\rightarrow$ (0.000,0.333,0.000)
HSE06	(0.500,0.000,0.000) $\rightarrow$ (0.000,0.000,0.000)

Table 7.5: Minimum gap between k-point in valence band and conduction band in SQS B from PBE, SCAN and HSE06

In table 7.5 we list the transition between the highest occupied k-state in the valence band and lowest unoccupied k-state in the conduction band for SQS B with PBE, SCAN and HSE06 respectively. We observe that all 3 functionals find different band gaps. A concerning factor is that the highest energy k-point in the valence band from PBE calculations (0.250, 0.000, 0.250) is not included in the HSE06 calculation with the narrow mesh of 2x2x2 k-points. Thus one may suspect that the HSE06 calculation overlook the minimum transition and hence return a enlarged band gap instead. This could be the case in  $E_{G,A}^{up}$  and  $E_{G,B}^{dw}$  where HSE06 predicts much larger values to PBE. However without an experimental baseline we can not conclude that this is the case. As in the other instances we find that HSE06 produce similar or lower band gaps compare to PBE despite of the smaller number of k-points.

As stated in section 6.2, we did not manage to converge hybrid calculations with the tetrahedron method, and overcame this problem by first calculating the charge density with Gaussian smearing and utilize the density to expedite TBC HSE06 calculations. The respective band gaps from these methods are displayed in table 7.6 for the five SQSs of the (CrFeMnNi)Si<sub>2</sub> system. Here we calculate the band gap from the eigenvalues at different cutoff occupancy *occ* to highlight the part of defect states. Gaussian smearing was tested with smearing width *sigma* equal to 0.05 eV and 0.005 eV.

SQS	Smearing (type) width (eV)	$E_G^{up,eigen}$ (0.5) (eV)	$E_G^{dw,eigen}$ (0.5) (eV)	$E_G^{up,eigen}$ (0.01) (eV)	$E_G^{dw,eigen}$ (0.01) (eV)	$E_G^{tot,eigen}$ (0.5) (eV)	$E_G^{tot,eigen}$ (0.01) (eV)
A	Gaussian (0.05)	0.7837	0.1493	-	0.2984	0.1493	0.2984
	Gaussian (0.005)	0.2117	0.1013	-	-	0.1013	-
	TBC	0.7084	0.0261	-	-	0.0261	-
B	Gaussian (0.05)	0.2783	0.1702	0.2988	0.3136	0.1506	0.2979
	Gaussian (0.005)	0.2838	0.1823	-	-	0.1801	-
	TBC	0.2855	0.1819	-	-	0.1807	-
C	Gaussian (0.05)	0.1078	0.1066	0.2405	0.1839	0.0650	0.1839
	Gaussian (0.005)	0.1304	0.0222	-	-	0.0222	-
	TBC	0.1744	0.0328	-	-	0.0196	-
D	Gaussian (0.05)	0.3661	0.0592	-	0.1872	0.0592	0.1872
	Gaussian (0.005)	0.3736	0.0723	-	-	0.0723	-
	TBC	0.3780	0	-	0.2665	0	0.2637
E	Gaussian (0.05)	0.6653	0.1439	-	0.1675	0.1439	0.1675
	Gaussian (0.005)	0.5825	0.1211	-	-	0.1211	-
	TBC	0.5476	0.0133	-	-	0.0133	-

Table 7.6: Band gap from HSE06 calculations with Gaussian smearing and smearing width  $\sigma$  equal to 0.05 and 0.005, and the tetrahedron method (TBC). "-" means unchanged

From table 7.6 we observe that the presence and affect of defect states as discussed in section 7.2.1 is only present with Gaussian ( $\sigma = 0.05eV$ ). Alike the previous cases, we find here finite band gaps despite of defect states. By comparing  $E_G^{\text{up}}$  and  $E_G^{\text{dw}}$  at  $occ = 0.5$  and  $occ = 0.01$ , the defects appear to have a lesser role in spin up, as par SQS C the band gap in spin up is either consistent or only marginally different between the defect band gap and the hypothetical defect less band gap.  $E_G^{\text{dw}}$  on the other hand increase significantly by removing the defect states. The Gaussian smearing method is generally in better agreement with TBC at lower smearing width. But even in this case we find several dissimilarities. In A and E  $E_G^{\text{dw}}$  is larger with the Gaussian method, additionally  $E_G^{\text{up}}$  is much lower in SQS A. Furthermore the band gap of SQS D with HSE06 is with TBC in good agreement with the half-metallic compound found with PBE, meanwhile the Gaussian method ( $\sigma = 0.005eV$ ) predicts a semiconductor with band gap equal to  $0.07eV$ . In this project we have based our choice of numerical smearing on the advice on the VASP manual that state that for accurate total energies and density of states in semiconductors one should opt for the tetrahedron method [14]. However since our system is comprised of metals as well as Si, we include the results from utilizing Gaussian smearing. There are of course many more factors that affect the accuracy and reliability of both methods, but these are outside the scope of this project.

The fact that all 3 functionals and five SQS in majority agree on the presence of a band gap is in itself an overwhelmingly positive result that allow us to state with high certainty that the potential high-entropy silicide (CrFeMnNi)Si<sub>2</sub> is in fact a semiconductor or possibly a half-metal based on the observed spin polarization and the utmost stable configuration. Regarding the 3 functionals applied in this project, we experience best cohesion between PBE and HSE06 that both agree on a spin up polarization of the band gap, while SCAN predicts more symmetric band gaps. This can also be seen from the magnetic moment, with PBE and HSE06 the final magnetic moment (per atom) is  $0.083 \mu_B$  across all SQSs, with SCAN this is reduced to half the amount. In the nonmagnetic  $\beta$ -FeSi<sub>2</sub> structure we find better agreement between PBE and SCAN. Both correctly predict that the material is nonmagnetic, however compared to the experimental value of about 0.85 eV and the PBE band gap of 0.65 eV, we get a smaller band gap of 0.61 eV with SCAN. Thus the SCAN functional does not necessarily result in increased accuracy over PBE even in the nonmagnetic material. To conclude this section on the band gap (CrFeMnNi)Si<sub>2</sub>, when studying the band gap with DFT, particularly PBE is well known to underestimate the band gap of the real material as in FeSi<sub>2</sub>. Therefore a band gap found with PBE would with high probability be replicated/increased in the real material. In the following sections and cases we will heavily emphasize the PBE functional to determine the band gap from both the fast and reliable use in addition to the point mentioned above. Furthermore from our experiences in this project in conjunction with the lack of literary support the SCAN function look to be ill-equipped for accurate band gaps. While the HSE06 functional is often to computationally expensive and

troublesome to converge for the structures in this project.

## 7.2.4 Pair distribution functions

The pair distribution functions of SQS D and B can be seen below in figure 7.10. We analyze the PDFs of the utmost stable configuration (SQS D) side by side to SQS B to investigate distinctions between the half-metallic structure and the semiconducting structure (B).

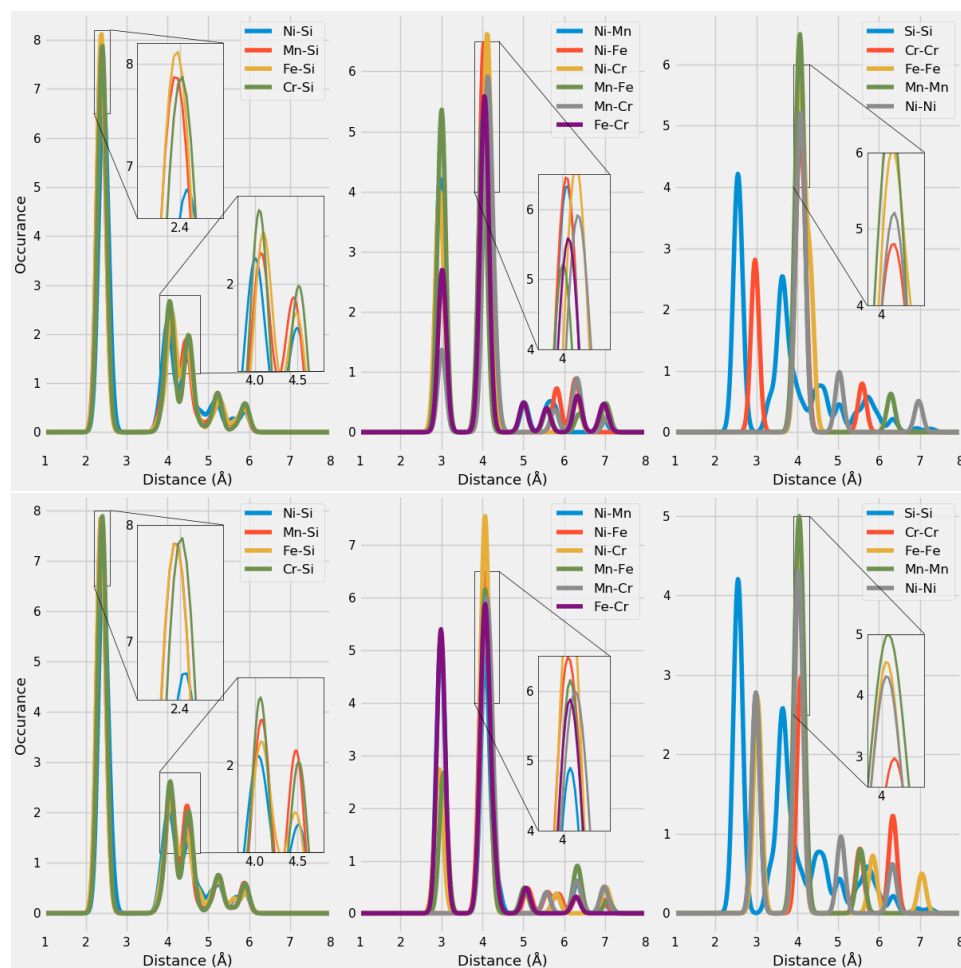


Figure 7.10: Pair distribution functions of SQS D (top) and B (bottom)

With the aid of the ICSD (**insert citation**), we can compare the PDFs in figure 7.10 to the expected PDFs based on a large number of experimental compounds. As our compound contains a total of 15 different bonds, comparing each one to the ICSD values would be an exhaustive process. According to the ICSD, the preferred bond-length of TM-Si bonds is observed at two values, with the shorter length the most occurring. Specifically Fe-Si between 2.25-2.75 Å and 4-5 Å, Mn-Si at 2.25-2.75 Å and 3.5-5 Å, Ni-Si between 2.25-2.5 Å and 3.85-5 Å, and finally Cr-Si between 2.35-2.65 Å and 4-5 Å. Clearly, the PDFs of the SQSs are in good agreement with the listed values of TM-Si bonds. The relative occurrence of the bonds

between SQS D and B are mostly consistent, other than marginally reduced Fe-Si occurrence at 2.4 Å in B.

In contrast, we observe several distinctions between TM-TM bonds in SQS D and B, for example Mn-Fe, Cr-Fe, and Ni-Mn bonds. This is simply a consequence of how the SQSs are generated, the silicon atoms are placed as before in the new supercells, but the TM elements are "randomly" distributed. Thus, it's reasonable that we would find the major differences between TM-TM bonds. Recalling that Mn had a distinct presence in spin down around  $E_F$  in SQS D, we observe that this structure compared to SQS B have a preference of Mn-Fe bonds at 3 Å and show larger occurrence of Mn-Mn bonds at 4 Å. However the differences between PDFs are difficult to relate to the observed properties. Firstly because of the sheer number of total bonds in the structures, and secondly considering the uniqueness of each SQS paired with the uncertainties regarding the stability.

### 7.2.5 Charge density

Below we include the calculated charge density (with PBE) of the different configurations. The half-metallic configuration (D) appear more metallic by a greater number of delocalized electronic charges compared to the semiconducting configurations A, B, and E. The charge density of SQS C is found in appendix A.3.

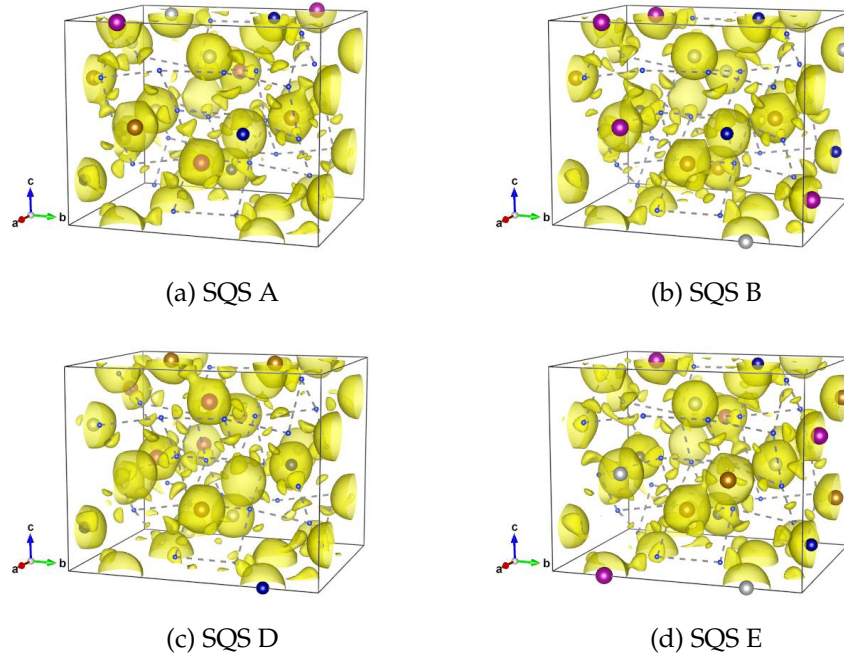


Figure 7.11: Charge density in SQS A, B, D and E of  $\text{Cr}_4\text{Fe}_4\text{Mn}_4\text{Ni}_4\text{Si}_{32}$



### 7.2.6 SQS size

Above we have presented the results of a high-entropy silicide (CrFeMnNi)Si<sub>2</sub> investigated by 5 48-atom SQSs with a volume of 700 Å<sup>3</sup>. This intermediate size allowed us to apply different XC-functionals, and a broad study of different compositions which we will discuss in the next section. However the application of the SQS method to HEAs is not necessarily straightforward as we discussed in section 4.3. The most pressing concern is the size of the SQS model and if it's sufficient enough to correctly model the disordered multi-component structure. In this section we will evaluate this factor by studying the difference between the 48 atom SQSs discussed above to that of 96 and 192-atom SQSs with volume 1200 Å<sup>3</sup> and 2400 Å<sup>3</sup> respectively. The computational cost of the 3 sizes are included below in figure 7.11 in terms of the number of CPU hours.

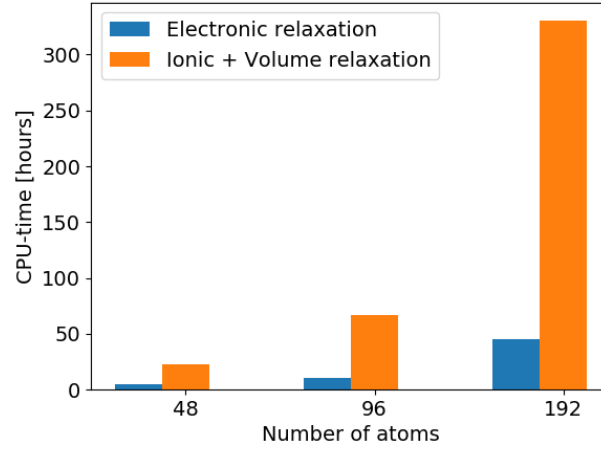


Figure 7.12: CPU time of 48, 96 and 192-atom SQSs of (CrFeMnNi)Si<sub>2</sub>

Alike the 48-atom model, the 96 and 192-atom SQS were tested by 5 unique configurations. In table 7.7 we report the mean and standard deviation from the set of configurations for all three sizes, with respect to the total energy per atom and final magnetic moment per atom, in addition to the formation energy of the mean total energy.

SQS size	Toten (eV)		Mag ( $\mu_B$ )		$E_{FPA}$ (eV)
	mean	std	mean	std	mean
48 atoms	- 6.6105	..	0.0833	0.0000	-0.292
96 atoms	- 6.6092	0.0021	0.0708	0.0114	-0.292
192 atoms	- 6.6123	0.0022	0.0761	0.0171	-0.295

Table 7.7: Total energy, magnetic moment and formation energy of 48, 96 and 192 atom SQSs of (CrFeMnNi)Si<sub>2</sub>

As seen from table 7.7 the total energy, magnetism and corresponding formation energy show very minimal variation between all three sizes, thus the 48-atom model is well converged. On the other hand we observe that the larger models contain larger deviation between configurations, this can be expected given the total number of atoms that can vary between configurations. The band gap corresponding to SQSs of each size are listed in table 7.8. First and foremost the band gap is evident in all three and exhibits analogous spin polarization, however the band gap appears to be less frequent and smaller in the larger structures.

SQS size	SQS	$E_G^{up,eigen}(0.5)$ (eV)	$E_G^{dw,eigen}(0.5)$ (eV)	$E_G^{tot,eigen}(0.5)$ (eV)
48 atoms	A	0.0815	0.0521	0.0281
	B	0.2932	0.0523	0.0523
	C	0.2355	0.0343	0.0343
	D	0.3386	0	0
	E	0.3078	0.0495	0.0495
96 atoms	A	0.1705	0.0442	0.0367
	B	0.1386	0.0270	0.0270
	C	0.1347	0.0363	0.0075
	D	0.0892	0.0398	0.0398
	E	0.1610	0	0
192 atoms	A	0.1197	0.0321	0.0321
	B	0.1444	0	0
	C	0.1867	0	0
	D	<i>0.0478</i>	<i>0.0339</i>	0
	E	<i>0.0131</i>	<i>0.0184</i>	<i>0.0131</i>

Table 7.8: Band gap of SQSs of 48, 96 and 192-atoms of (CrFeMnNi)Si<sub>2</sub>. The names are arbitrary, ie A in 48 does not equal A in 96 or A in 192. The values listed in *cursive* indicate a defect band gap.

Equivalent to structure D in the 48 atom SQS we find that the 0 value in SQS E in the 48 atom model suffers from defect states, and  $E_G^{dw,eigen}(0.90,0.10) = 0.016$  eV. The same is true for SQS B and C (192), but require  $occ = 0.999, 0.001$  to yield a finite band gap in spin down. The band gap in SQS D and E (192) on the other hand is finite at  $occ = 0.5$  but can be enlarged from increasing  $occ$ , as we described for the Gaussian ( $\sigma = 0.05$  eV) calculations previously. In SQS D (192-atoms)  $E_G^{up,eigen}(0.99) = 0.075$  eV and  $E_G^{dw,eigen}(0.01) = 0.05$  eV and similarly  $E_G^{up,eigen}(0.99) = 0.05$  eV, and  $E_G^{dw,eigen}(0.01) = 0.048$  eV in SQS E (192-atoms). In such cases where the eigenvalues inclusive of defect states return a finite band gap, the density of states does not. This is seen in figure 7.12 for SQS E in the 192-atom model that clearly have nonzero DOS at  $E_F$  in both spins.

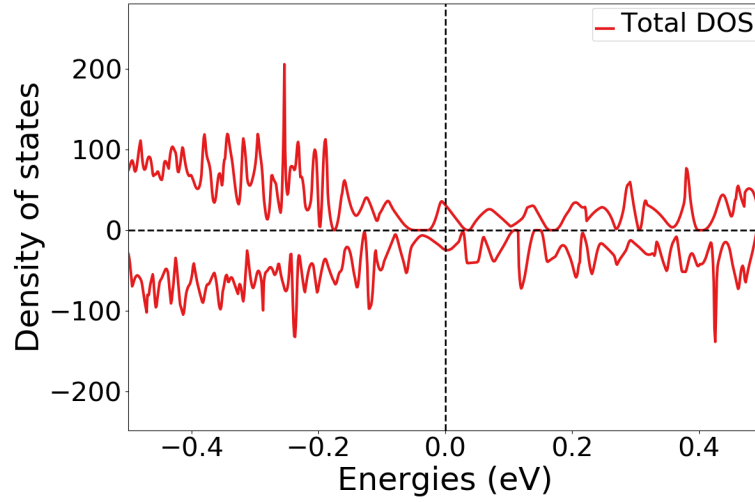


Figure 7.13: Density of states of SQS E 192 atom SQS.

One could wonder if the very narrow band gap from the eigenvalues of 0.01 eV is subject to numerical precision in the DOS. But on the grounds of the small value we calculated the DOS in this case by 20000 points over the energy range -12 eV to 12 eV which results in a resolution of about 8 points per 0.01 eV. In other words this should not be a factor of the DOS in figure 7.12.

Drawing any conclusion on the band gaps is difficult seeing as we find very different results within all 3 sizes. The utmost stable SQSs suggests that the band gap converge towards a small or possible non-existent band gap with increasing SQS size. On the other hand we also find evidence of large band gaps in the larger cells in less stable configurations. This goes back to section 3.3 where we mentioned that one particular difficulty of the SQS method is the large number of possible atomic configurations of one composition. We should note that for the sake of comparison, we conducted the calculations of the larger SQSs with identical computational parameters as the 48-atom models, this could affect the accuracy of the larger structures.

Looking at the pair distribution functions of the utmost stable SQS in each size (figure 7.13), we observe that short-range interactions is well represented and identical across all three models. The distinctions between preferences as discussed in section 7.2.4 is most likely a product of the uniqueness of the SQSs more so than the size. On the other hand the larger SQSs clearly provide a better description of large-range interactions, that is not nearly as present in the smaller supercell. But as seen from the minimal variation of the values in table 7.7 between the 3 models, in accordance with the fundamental philosophy of the SQS method that the functional properties are determined primarily from short-range interactions in the lattice. Thus, despite the fact that the larger SQSs offer improvement over the smaller SQSs, the gain is not justified by the cost. On the other hand, the SQS size looks to have more of an impact on the band gap of the material. But this could just as easily be a consequence of the sensitivity of the band

gap to the particular atomic configuration as seen in table 7.8.

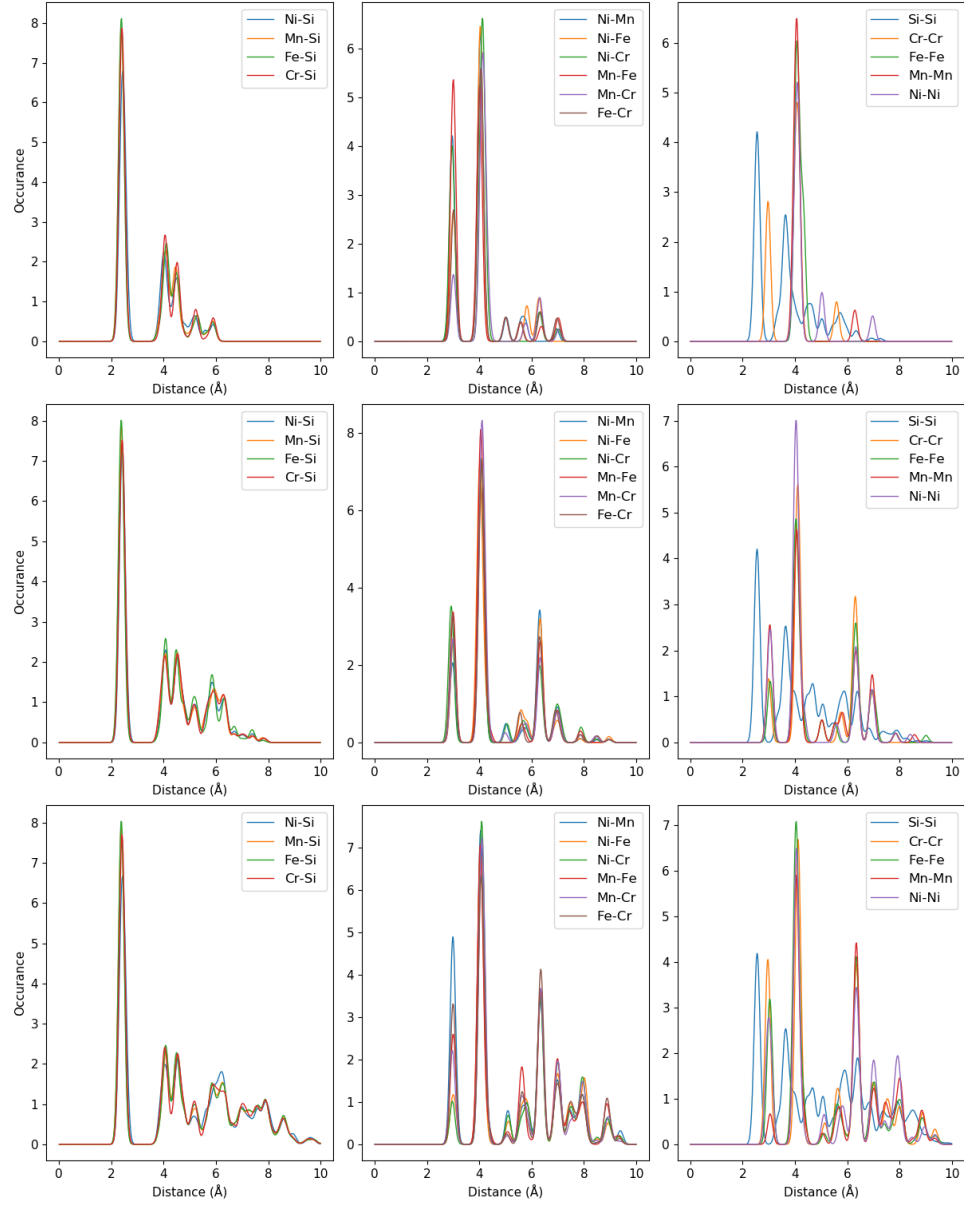


Figure 7.14: Pair distribution functions of (CrFeMnNi)Si<sub>2</sub> (top) 48-atom SQS, (middle) 96-atom SQS, (bottom) 192-atom SQS.

## Chapter 8

# Alternative compositions

Up until this point we have looked in detail at the high-entropy silicide (CrFeMnNi)Si<sub>2</sub>. In this chapter we will broaden our search of compositions based on the  $\beta$ -FeSi<sub>2</sub> structure. First, we will look at various compositions inside the quaternary phase diagram of Cr, Fe, Mn and Ni, followed by compositions where chromium, manganese or nickel are replaced by cobalt or titanium.

### 8.1 Exploring the quaternary phase diagram

In this section, we aim to expand our search of this diagram by generating SQSs of the 48 atom model slightly away from equimolar distribution of 3d elements. The compositions we test are listed in table 8.1, with corresponding total energy, magnetic moment and formation energy in the familiar format. Ideally each composition would differ only by one element to provide a clear view of each direction in the phase diagram, but the TDEP implementation insist in reducing Nickel to stay consistent with the 48 atom supercell.

Composition	Toten (eV)		Mag ( $\mu_B$ )		$E_{FPA}$ (eV)
	mean	std	mean	std	mean
Cr <sub>3</sub> Fe <sub>3</sub> Mn <sub>7</sub> Ni <sub>3</sub> Si <sub>32</sub>	- 6.6947	0.0040	0.1375	0.0186	-0.300
Cr <sub>5</sub> Fe <sub>5</sub> Mn <sub>3</sub> Ni <sub>3</sub> Si <sub>32</sub>	- 6.6705	0.0030	0.1127	0.0223	-0.286
Cr <sub>5</sub> Fe <sub>3</sub> Mn <sub>5</sub> Ni <sub>3</sub> Si <sub>32</sub>	- 6.6852	0.0041	0.1375	0.0456	-0.271
Cr <sub>3</sub> Fe <sub>5</sub> Mn <sub>5</sub> Ni <sub>3</sub> Si <sub>32</sub>	- 6.6801	0.0036	0.0937	0.0209	-0.315
Cr <sub>3</sub> Fe <sub>3</sub> Mn <sub>3</sub> Ni <sub>7</sub> Si <sub>32</sub>	- 6.3921	0.0078	0.0159	0.0101	-0.285

Table 8.1: Summary composition diagram

In table 8.1 we observe that moving away from the equimolar system result in both less and more stable alloys. Clearly the most lowest formation energies (most stable) correspond to compositions rich in manganese and poor in chromium. Likewise the least stable compositions in table

8.1 contain either increased amounts of Cr or reduced amounts of Mn compared to the equimolar system. In the equimolar composition the magnetic moment was attributed to primarily Cr and Mn atoms in the lattice. In table 8.1 we observe similarly that compositions rich in Cr and Mn exhibits the largest magnetic moments and vice versa. The band gaps of the respective compositions in five unique SQSs can be seen in table 8.2 below, calculated with PBE GGA.

Composition	SQS	$E_G^{\text{up, eigen}}(0.5)$ (eV)	$E_G^{\text{dw, eigen}}(0.5)$ (eV)	$E_G^{\text{tot, eigen}}(0.5, 0.5)$ (eV)
$\text{Cr}_3\text{Fe}_3\text{Mn}_7\text{Ni}_3\text{Si}_{32}$	<b>A</b>	0.3390	0	0
	<b>B</b>	0.4745	0	0
	C	0.1342	0	0
	D	0.1950	0.0063	0.0063
	E	0.4211	0	0
$\text{Cr}_5\text{Fe}_5\text{Mn}_3\text{Ni}_3\text{Si}_{32}$	A	0.003	0	0
	<b>C</b>	0.21	0	0
	D	0.0674	0.0413	0.0372
	E	0.362	0	0
$\text{Cr}_5\text{Fe}_3\text{Mn}_5\text{Ni}_3\text{Si}_{32}$	<b>A</b>	0.2082	0	0
	B	0.4053	0	0
	C	0.4659	0	0
	D	0.0843	0.0121	0.0121
	E	0.3008	0	0
$\text{Cr}_3\text{Fe}_5\text{Mn}_5\text{Ni}_3\text{Si}_{32}$	A	0.3922	0	0
	C	0.1285	0	0
	<b>D</b>	0.2595	0.1004	0.1004
	E	0.3591	0.1003	0.0848
$\text{Cr}_3\text{Fe}_3\text{Mn}_3\text{Ni}_7\text{Si}_{32}$	A	0	0	0
	B	0	0	0
	C	0	0	0
	D	0	0	0
	<b>E</b>	0.04	0	0

Table 8.2: Band gaps of various compositions of  $(\text{CrFeMnNi})\text{Si}_2$ . Most stable SQS of a set is highlighted in bold text, defect/impurity band gap are listed in cursive. Some SQSs were excluded from the table due to unsuccessful calculations.

From table 8.2 we observe that most compositions are half-metals alike the equimolar system with a spin up polarization. Each composition show large variation between configurations. We note  $E_{G, \text{max}}^{\text{up}} \approx 0.5$  eV and  $E_{\text{min}}^{\text{up}} \approx 0.1$  eV in both  $\text{Cr}_3\text{Fe}_3\text{Mn}_7\text{Ni}_3\text{Si}_{32}$  and  $\text{Cr}_5\text{Fe}_3\text{Mn}_5\text{Ni}_3\text{Si}_{32}$ , and further  $E_{G, \text{max}}^{\text{up}} \approx 0.4$  eV and  $E_{\text{min}}^{\text{up}} \approx 0.1$  eV in  $\text{Cr}_3\text{FeMn}_5\text{Ni}_3\text{Si}_{32}$ . In all three of these compositions the proportion of manganese is increased relative

to the equimolar system, and two out of the three compositions contain reduced amounts of chromium. Looking at the two compositions with the least indication of a band gap  $\text{Cr}_5\text{Fe}_5\text{Mn}_3\text{Ni}_3\text{Si}_{32}$  and  $\text{Cr}_3\text{Fe}_3\text{Mn}_3\text{Ni}_7$ , these contain reduced amounts of manganese. Thus, based on the few compositions tested in this experiment we can state a relation of the band gap mainly to manganese, but also chromium.

Based on the utmost stable configuration of each composition, we observe very encouraging results in the  $\text{Cr}_3\text{Fe}_3\text{Mn}_7\text{Ni}_3\text{Si}_{32}$  composition with the largest  $E_G^{\text{up}}$  of the set of configurations, likewise the most stable SQS of the  $\text{Cr}_3\text{Fe}_5\text{Mn}_5\text{Ni}_3\text{Si}_{32}$  composition is a semiconductor with a total band gap of about 0.1 eV. In the composition  $\text{Cr}_5\text{Fe}_5\text{Mn}_3\text{Ni}_3\text{Si}_{32}$  the most stable SQS predicts a defect or impurity band gap as we discussed previously where the eigenvalues return a finite band gap despite of defect states. However we have not been able to investigate the nature and effect of this impurity band gap to further extent, likewise for the similar impurity gaps listed in table 8.2 and the 0 band gaps in spin down. Below in figures 8.1 and 8.2 we include the projected density of states around  $E_F$  of the utmost stable SQS of each composition. Because we only include and discuss the most stable SQS, the features of these figures can be subject to the uniqueness of that particular SQS rather than a distinct feature of the exact composition, but as stated previously the most stable configuration provide the most likely properties of the composition within the scope of this project.

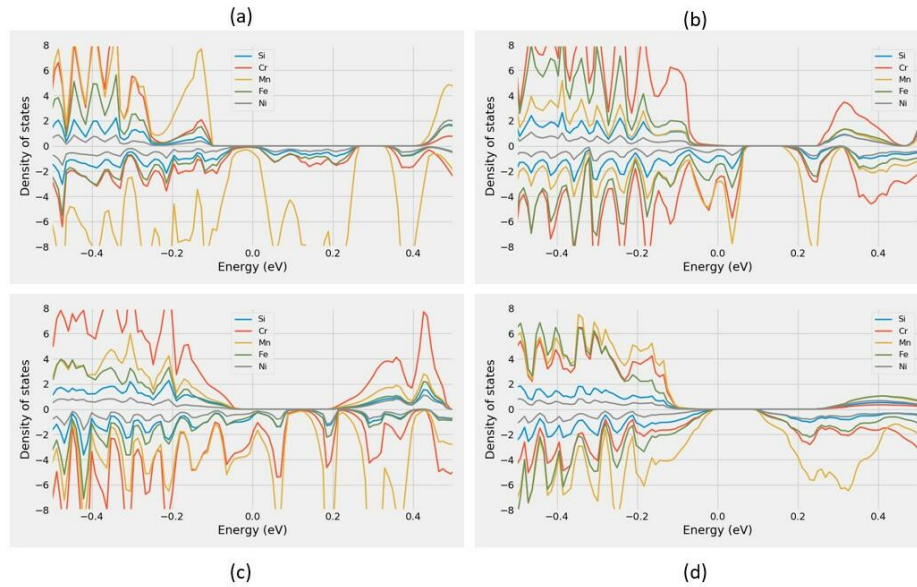


Figure 8.1: Projected density of states of (a)  $\text{Cr}_3\text{Fe}_3\text{Mn}_7\text{Ni}_3\text{Si}_{32}$  (SQS B), (b)  $\text{Cr}_5\text{Fe}_5\text{Mn}_3\text{Ni}_3\text{Si}_{32}$  (SQS C), (c)  $\text{Cr}_5\text{Fe}_3\text{Mn}_5\text{Ni}_3\text{Si}_{32}$  (SQS A), (d)  $\text{Cr}_3\text{Fe}_5\text{Mn}_5\text{Ni}_3\text{Si}_{32}$  (SQS D)

The PDOSs is in good agreement with the listed values in table 7.2.  $\text{Cr}_3\text{Fe}_3\text{Mn}_7\text{Ni}_3\text{Si}_{32}$  and  $\text{Cr}_5\text{Fe}_3\text{Mn}_5\text{Ni}_3\text{Si}_{32}$  both display sizable band gaps in

spin, while figure 8.1 d point to a total band gap around 0.1 eV for SQS D of  $\text{Cr}_3\text{Fe}_5\text{Mn}_5\text{Ni}_3\text{Si}_{32}$ . On the other hand we observe as for the 192-atom SQS a dissimilarity between the density of states band gap in  $\text{Cr}_5\text{Fe}_5\text{Mn}_3\text{Ni}_3\text{Si}_{32}$  SQS C (figure 8.1 b) and the eigenvalue (impurity) band gap listed in table 7.2. This can be better understood by figure .. in appendix .. that display a zoomed in DOS that clearly show small finite values at  $E_F$  in spin up. This DOS may resemble that of a n-doped material where the Fermi energy is pushed up in energy.

In figure 7.7 we saw that manganese distinctly occupied states in the spin down channel around  $E_F$  and was a key contributor as to why the spin down channel of  $(\text{CrFeMnNi})\text{Si}_2$  was metallic in the utmost stable SQS. This is also largely the case in the compositions shown above in figure 8.1 and 8.2, and is particularly evident in figure 8.1 where Mn dominate the spin down states around  $E_F$  in the  $\text{Cr}_3\text{Fe}_3\text{Mn}_7\text{Ni}_3\text{Si}_{32}$  composition. By reducing the number of Mn we still find that the Mn states prohibit the band gap in spin down, as seen in figure 8.1 b. In the chromium rich compositions plotted in figures 8.1 b and c, we observe that also Cr states prohibit the spin down band gap, and dominate states near  $E_F$  in spin up as well. Contrary, in the  $\text{Cr}_3\text{Fe}_3\text{Mn}_3\text{Ni}_7\text{Si}_{32}$  composition plotted in figure 8.2, we do not observe any distinct peaks of elements, but rather consistent small finite DOS around  $E_F$  in all elements. The sole composition with clear evidence of a spin down gap is from the chromium poor system plotted in figure 8.1 d. Also in this structure we see that the effects of Mn around  $E_F$  is dominant in spin down from the relative large amounts of Mn, but in comparison to the other composition these states are pushed away from the Fermi energy.

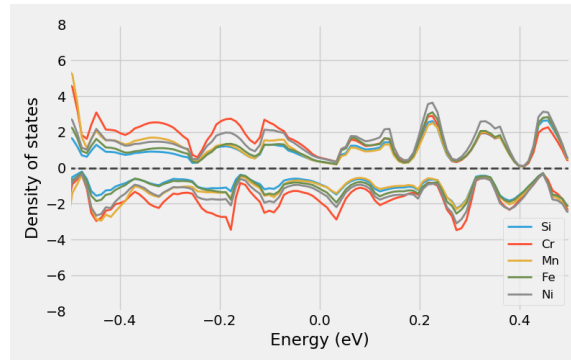


Figure 8.2: Projected density of states of  $\text{Cr}_3\text{Fe}_3\text{Mn}_3\text{Ni}_7\text{Si}_{32}$  around  $E_F$

An important factor of these results is that because each composition alters simultaneous elements, interpreting and relating the results to a particular alteration is challenging. For example, is the result of the  $\text{Cr}_5\text{Fe}_3\text{Mn}_5\text{Ni}_3\text{Si}_{32}$  permutation a consequence of less Fe or increments to both Cr and Mn? Furthermore is the large band gap in spin up of  $\text{Cr}_3\text{Fe}_3\text{Mn}_7\text{Ni}_3\text{Si}_{32}$  a product of increasing manganese or reducing the other elements. From the comparatively large gaps in spin up of  $\text{Cr}_3\text{Fe}_3\text{Mn}_7\text{Ni}_3\text{Si}_{32}$  and  $\text{Cr}_3\text{Fe}_5\text{Mn}_5\text{Ni}_3\text{Si}_{32}$  and the more present Cr states in spin up in the Cr rich permutations we here conclude that the band gap



is related to lessening of chromium, more so than other effects. However we see from both  $\text{Cr}_5\text{Fe}_5\text{Mn}_4\text{Ni}_3\text{Si}_{32}$  and  $\text{Cr}_3\text{Fe}_3\text{Mn}_3\text{Ni}_7\text{Si}_{32}$  (figure 8.2) in addition to the manganese rich composition that Mn plays a vital role on the band gap of these structures. It's clear that the  $\text{Cr}_3\text{Fe}_5\text{Mn}_5\text{Ni}_3\text{Si}_{32}$  alloy manage to strike a balance between 3d elements that results in a specific interplay and correspondingly very promising properties. It would have been beneficiary to look at for example the pair distribution functions and compare to the equimolar system, but from the factors discussed in section 7.2.4 we leave this to future work.

As stated before, we relied on the PBE GGA functional to determine the band gap in this part from its reliability and favorably computation cost. However we have conducted calculations with SCAN and HSE06 on some of the more promising structures. For instance in SQS D of  $\text{Cr}_3\text{Fe}_5\text{Mn}_5\text{Ni}_3\text{Si}_{32}$  we get lower values in both spin up and down with SCAN, specifically  $E_{G, \text{SCAN}}^{\text{up}} = 0.21$  eV and  $E_{G, \text{SCAN}}^{\text{dw}} = 0.08$  eV, and on the other hand HSE06 predicts  $E_{G, \text{HSE06}}^{\text{up}} = 0.53$  eV and  $E_{G, \text{HSE06}}^{\text{dw}} = 0$  eV. In SQS B of  $\text{Cr}_3\text{Fe}_3\text{Mn}_7\text{Ni}_3\text{Si}_{32}$  we observe very different outcomes. With SCAN we get a small band gap in spin down of about 0.002 eV and 0 in spin up, likewise the HSE06 band gap of this structure is  $E_{G, \text{HSE06}}^{\text{up}} = 0.08$  eV and  $E_{G, \text{HSE06}}^{\text{dw}} = 0.11$  eV, opposed to  $E_{G, \text{PBE}}^{\text{up}} = 0.47$  eV and  $E_{G, \text{PBE}}^{\text{dw}} = 0$  eV. Further the HSE06 band gap is in fact an impurity band gap, with  $E_{G, \text{HSE06}}^{\text{up, eigen}}(0.01) = 0.18$  eV and  $E_{G, \text{HSE06}}^{\text{dw, eigen}}(0.01) = 0.16$  eV.

## 8.2 High entropy silicides with cobalt/titanium

In similar fashion to the preceding section, we begin by presenting the new high-entropy silicides by the mean and standard deviation of the total energy and magnetization of 5 unique SQSs of each alloy in table 8.3. The compositions we have tested are deliberate combinations intended to investigate the role elements in the  $(\text{CrFeMnNi})\text{Si}_2$  system, by introducing Co/Ti at the cost of different elements. Note that the alloys contain a total of 48 atoms as before, based on the  $\beta$ - $\text{FeSi}_2$  unit cell and equimolar distribution of 3d elements.

Composition	Toten (eV)		Mag ( $\mu_B$ )		$E_{FPA}$ (eV)
	mean	std	mean	std	mean
$\text{Cr}_4\text{Fe}_4\text{Co}_4\text{Ni}_4\text{Si}_{32}$	- 6.4655	0.0056	0.0083	0.0155	-0.308
$\text{Co}_4\text{Fe}_4\text{Mn}_4\text{Ni}_4\text{Si}_{32}$	- 6.4731	0.0046	0.0000	0.0000	-0.355
$\text{Cr}_4\text{Fe}_4\text{Ti}_4\text{Ni}_4\text{Si}_{32}$	- 6.4217	0.0087	0.0305	0.0293	-0.209
$\text{Cr}_4\text{Fe}_4\text{Mn}_4\text{Ti}_4\text{Si}_{32}$	-6.6994	0.0071	0.1142	0.0641	-0.199
$\text{Cr}_4\text{Fe}_4\text{Mn}_4\text{Co}_4\text{Si}_{32}$	-6.7687	0.0034	0.1331	0.0326	-0.323

Table 8.3: Overview new compositions

In terms of the formation energy, we observe that cobalt evidently yield

the utmost stable alloys from the tested compositions, with (CoFeMnNi)Si<sub>2</sub> at the top and (CrFeCoNi)Si<sub>2</sub> at the bottom. On the other side, both (CrFeTiNi)Si<sub>2</sub> and (CrFeMnTi)Si<sub>2</sub> where we introduce titanium in place of manganese and nickel respectively, result in the overall least stable compositions. A precise physical interpretation of the stability between compositions is challenging from the shallow analysis in this project, but we do note that the two most stable alloys consist of the most chemically similar elements with respect to properties such as the electronegativity and atomic size. Following the least stable alloys are comprised of the most chemically dissimilar elements. This is in good agreement with the discussion in section 2.2 regarding phase formation of high-entropy alloys. Additionally, in the compositions discussed in the previous section we found that the most stable composition was Cr<sub>3</sub>Fe<sub>5</sub>Mn<sub>5</sub>Ni<sub>3</sub>Si<sub>32</sub> where the Cr proportion was lessened. In conjunction with the results of the titanium we thus may suspect that smaller elements are ill-suited in this structure.

In line with the other compositions studied in this project, the magnetization is clearly related to chromium and manganese also in this case. This is seen by the overall lowest magnetic moments in the two compositions without these elements, and reversely the highest magnetic moments is found for compositions with both Cr and Mn. Comparing the magnetic moment of (CrFeCoNi)Si<sub>2</sub> and (CoFeMnNi)Si<sub>2</sub> it seems in our study that chromium is most responsible for the magnetic moment in these alloys. Furthermore we find that substituting Ni with both Ti and Co yields more magnetic compounds. As we have discussed previously, the uniqueness of each SQS makes it difficult to draw conclusion on the various properties. In table 8.4 below we list the magnetic moment of the utmost stable SQS in each alloy. Contrary to the mean value we find that (CrFeCoNi)Si<sub>2</sub> equal to (CoFeMnNi)Si<sub>2</sub> is nonmagnetic, moreover (CrFeMnTi)Si<sub>2</sub> are less magnetic relative to both (CrFeMnCo)Si<sub>2</sub> and (CrFeMnNi)Si<sub>2</sub>.

Composition	Magnetic moment ( $\mu_B$ )
Cr <sub>4</sub> Fe <sub>4</sub> Co <sub>4</sub> Ni <sub>4</sub> Si <sub>32</sub>	0
Co <sub>4</sub> Fe <sub>4</sub> Mn <sub>4</sub> Ni <sub>4</sub> Si <sub>32</sub>	0
Cr <sub>4</sub> Fe <sub>4</sub> Ti <sub>4</sub> Ni <sub>4</sub> Si <sub>32</sub>	0,0653
Cr <sub>4</sub> Fe <sub>4</sub> Mn <sub>4</sub> Ti <sub>4</sub> Si <sub>32</sub>	0,0785
Cr <sub>4</sub> Fe <sub>4</sub> Mn <sub>4</sub> Co <sub>4</sub> Si <sub>32</sub>	0,1666

Table 8.4: Final magnetic moment of the utmost stable SQS of each composition.

Thus, based on the utmost stable configurations we can state that replacing either Cr or Mn (with Co), removes the magnetic moment of the alloy. Furthermore we find that the magnetic moment is reduced when Ni is substituted with Ti, and increased by Co. However, while substituting manganese with Co yields a nonmagnetic alloy, Ti for Mn only slightly

reduces the magnetic moment.

In regards to the band gap, we find most to be metals. In table 8.5 we list the band gap of the utmost stable SQS of each composition, where the band gap is determined from the eigenvalues at different occupancy cutoff  $occ$  values to underline the effect of defect states. We find that increasing the criteria, in other words only consider states with occupancy above a certain threshold, the band gap become finite with  $occ = 0.1$  and converge to around  $0.02 - 0.06$  eV depending on composition at  $occ = 0.01$  and beyond.

Composition	$occ$	$E_G^{\text{up, eigen}}$ (eV)	$E_G^{\text{dw, eigen}}$ (eV)	$E_G^{\text{tot, eigen}}$ (eV)
CrFeCoNiSi <sub>2</sub>	0.5	0	0	0
	0.1	0.00095	0.0399	0.00095
	0.01	0.063	0.063	0.063
CrFeTiNiSi <sub>2</sub>	0.5	0.0067	0	0
	0.1	0.061	0.0087	0.0087
	0.01	0.061	0.037	0.037
CoFeMnNiSi <sub>2</sub>	0.5	0	0	0
	0.1	0.0037	0.0037	0.0037
	0.01	0.0268	0.0268	0.0268
CrFeMnTiSi <sub>2</sub>	0.5	0	0	0
	0.1	0.021	0.00049	0
	0.01	0.03	0.03	0.022
CrFeMnCoSi <sub>2</sub>	0.5	0.461	0	0
	0.1	0.607	0.0218	0.0218
	0.01	0.607	0.0245	0.0245

Table 8.5: The band gap in spin up/down and total of the utmost stable SQS in five high-entropy silicides based on  $\beta$ -FeSi<sub>2</sub>

The CrFeMnCoSi<sub>2</sub> composition exhibits a band gap of around 0.5 eV in spin up, contrary to the metallic compositions. We observe that the gap similar to the Cr<sub>5</sub>Fe<sub>5</sub>Mn<sub>3</sub>Ni<sub>3</sub>Si<sub>32</sub> composition and the the 192-atom SQS in section 7.2.5, is an impurity gap that contain a small number of defect states in addition to the finite gap. As was the case in these structures, the band gap in (CrFeMnCo)Si<sub>2</sub> display small nonzero DOS at the Fermi energy, as seen from the projected density of states in figure 8.3. As observed in the previous compositions, the PDOS in this alloy point to a severe number of manganese states in spin down at energies just above  $E_F$ , and further large number of Cr states right below  $E_F$  in spin up.

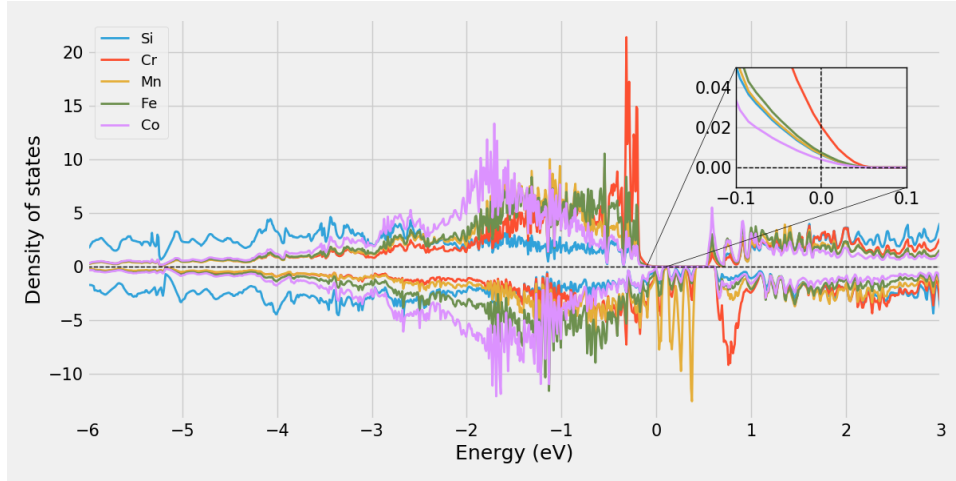


Figure 8.3: Projected density of states of  $(\text{CrFeMnCo})\text{Si}_2$ .

The PDOS of the other four alloys are included in figure 8.4 below. In agreement with the values listed in table 8.5 we observe clear indication of metallic structures, furthermore in agreement with the magnetic moments discussed previously.

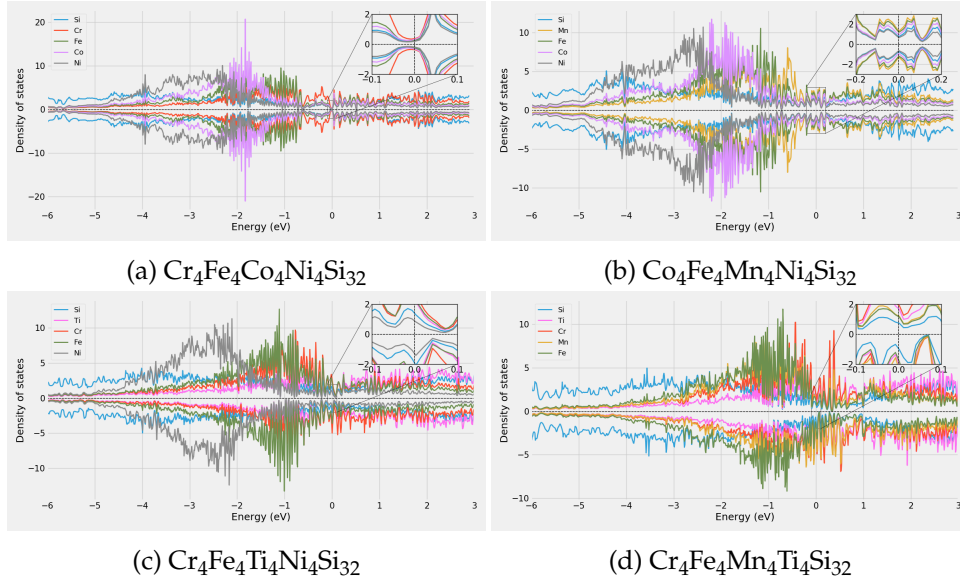


Figure 8.4: Projected density of states

Above we have evaluated the band gap of the different alloys based on the most stable configuration. Across all five configurations we find that the band gap is more or less consistent in  $(\text{CrFeCoNi})\text{Si}_2$ ,  $(\text{CrFeMnTiSi})_2$ ,  $(\text{CrFeTiNi})\text{Si}_2$  and  $(\text{CrFeMnCo})\text{Si}_2$ . The most interesting case is the  $\text{CoFeMnNiSi}_2$  alloy, where we observed very narrow total band gaps in two lesser stable configurations (SQS A and E) of 0.03 eV and 0.006 eV respectively. Opposite of the impurity gaps discussed above, these are apparent in the density of states plots, as seen in figure 8.5 below.

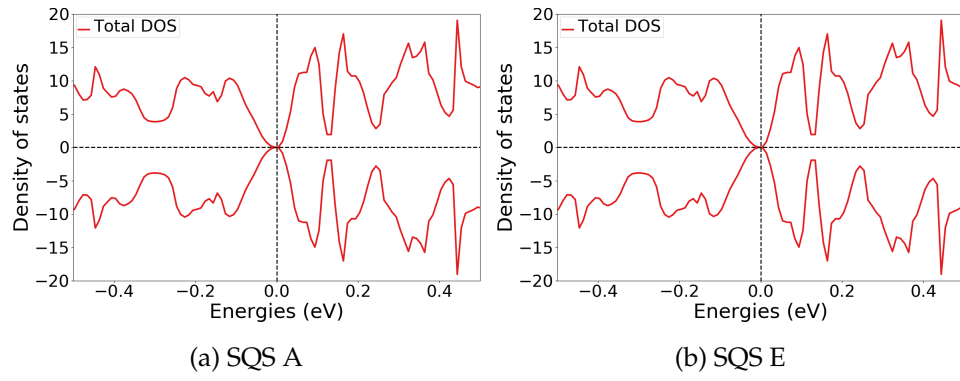


Figure 8.5: Density of states of two SQS A and E of  $(\text{CoFeMnNi})\text{Si}_2$ .

In addition to the tests discussed above, we attempted to replicate the  $\text{CrFeMnNi}$  system based on other silicides, such as hexagonal  $\text{CrSi}_2$ , trigonal  $\text{Fe}_2\text{Si}$ , and tetragonal and orthorhombic  $\text{Mn}_4\text{Si}_7$ , but found no indication of a band gap in these alloys. Furthermore we have tested a few alloys consisting of Sc, V, Zn, and Cu as well, but found no band gaps in these compositions either.

## **Part IV**

# **Conclusion and future work**

## Chapter 9

# Conclusion

High-entropy alloys has emerged as a rapidly growing interest in materials science from the large range of possibilities and flexibility. In this project we have set out to study the possibility of a narrow gap semiconducting high-entropy silicide with top of the line computational power and methods, in the prospect of discovering next-generation efficient thermoelectric materials. The materials in mind were based on the  $\text{FeSi}_2$  semiconductor, and modeled with the SQS method in the framework of DFT. To study the potential semiconductors we generated five distinct configurations of each composition and investigated the band gap, mainly with PBE GGA.

Our most successful effort was based around a 48-atom model of chromium, iron, manganese, and nickel in the  $\text{Cr:Fe:Mn:Ni:Si}$  system. In the equimolar composition  $(\text{CrFeMnNi})\text{Si}_2$  we observed large variation of the band gap between the five distinct configurations. In spin up, the band gap ranged from 0.08 - 0.34 eV. The most stable supercell was a half-metal, while the other four supercells displayed small spin down gaps between 0.03 eV and 0.05 eV as well. Calculations with SCAN and HSE06 produced unpredictable outputs that varied greatly between SQSs, and contained a larger degree of uncertainty compared to PBE. However, with HSE06 we found spin up band gaps of 0.55 eV and 0.71 eV in two respective supercells, and a total band gap of 0.18 eV in another. With SCAN we found total band gaps around 0.1 in three SQSs, one metal and one half-metal with a spin down band gap of 0.1 eV.

Following the equimolar composition, we conducted a brief exploration of the quasi-ternary phase diagram of this composition. Contrary to the equimolar system we found here more frequently half-metals. By analyzing the projected density of states we were able to relate the metallic spin down channel to a large dominant presence of manganese states around the Fermi energy. Inside the compositions that we tested, we found evidence for that there exists a positive relation between the band gap in this system, most notably in spin up, and compositions poor in chromium and/or rich in manganese. Specifically, we found two very positive compositions:  $\text{Cr}_3\text{Fe}_3\text{Mn}_7\text{Ni}_3\text{Si}_{32}$  and  $\text{Cr}_3\text{Fe}_5\text{Mn}_5\text{Ni}_3\text{Si}_{32}$ , where the most stable supercell of the former displayed a spin up band gap of 0.47 eV, and the latter a total band gap of 0.1 eV, with PBE.

Lastly, we tested various compositions where we introduced cobalt/titanium at the cost of either Cr, Mn or Ni. Based on the most stable configuration in each of these compositions, the only band gap we found in this experiment was a spin up band gap of 0.46 eV in  $(\text{CrFeMnCo})\text{Si}_2$ . By manually investigating the calculated eigenvalues of the different compositions, we were able to relate the metallic compounds to defect states in the band gap. This is a familiar term in random alloys, in which states at the band edges deviate slightly from completely full/empty occupancy. The effect and occurrence of defect states varied from composition to composition and supercell to supercell, for instance in the Cr:Fe:Mn:Ni:Si system, defects states was most prominent for spin down states, which resulted in several half-metals.

In relation to the initial hypothesis of this thesis, that high-entropy alloys are promising thermoelectric materials provided that we could locate narrow gap structures. Based on the values we have calculated for  $(\text{CrFeMnNi})\text{Si}_2$  alloy, the band gaps might be too small to become efficient thermoelectrics. On the other hand we have observed instances such as the HSE06 band gap of 0.18 in one configuration that would be well suited for thermoelectric application. Furthermore we could expect that the PBE band gaps reported in this project are under-estimations of the band gap, thus there is definitely potential. In terms of actual application though, one would need to perform a study directed at the related properties, such as the Seebeck coefficient, and electrical and thermal conductivity. From the observed large spin polarization of the band gap, a supplementary application of the Cr:Fe:Mn:Ni:Si alloys could be as spintronics [15]. In the  $(\text{CrFeMnNi})\text{Si}_2$  alloy we found a magnetic moment of  $0.083\mu_B$  in all five configurations. The local magnetic moments were largest for chromium atoms in the lattice, followed by manganese. This was found as a general trend in all alloys based on the  $\text{FeSi}_2$  structure.



## Chapter 10

### Future work

In future studies on this system, I would first and foremost try to resolve several of the uncertainties circling the results presented in this project. This would include a more thoughtful investigation of the true ground state of the  $(\text{CrFeMnNi})\text{Si}_2$  composition, by first testing multiple configurations and a larger number of SQS sizes to reduce variance and obtain a converged value of the band gap. Secondly, to decide on the most representative configuration we should have put more efforts into correctly/optimally specify the magnetic configuration of each SQS, and study excited states of the alloys to account for entropic contributions to the stability. Moreover, a test of different crystal structures in addition to the orthorhombic CMCE space group of the  $(\text{CrFeMnNi})\text{Si}_2$  alloy should be done, as the local minima method of DFT does not guarantee that this is the most stable conformation of the alloy.

The overarching motivation of this thesis have been to simply locate a band gap in high-entropy silicides, which by no means have been simple. However, now that we have located such a compound, in future work we would like to devote more effort into specifically analyze the band gap. Potentially try to plot and analyze the band structure of the alloy and qualitatively study the band gap by different functionals. Furthermore, we performed only a very limited search of the quasi-ternary phase diagram of the Cr:Fe:Mn:Ni:Si system, but found promising results in the direction of less chromium and more in manganese. Thus, a future study of more deliberate compositions in these directions would also be interesting. Provided that these results yielded positive outcomes of the band gap, suitable for thermoelectric application, future work could focus on a complete study of this material as a thermoelectric, and consider factors such as the Seebeck coefficient and electrical and thermal conductivity.

# Bibliography

- [1] termoelektrisitet. *Velkommen til en termoelektrisk verden!* nor. Nov. 2013. URL: <https://termoelektrisitet.no/2013/11/24/velkommen-til-en-termoelektrisk-verden/> (visited on 24/11/2013).
- [2] Wikipedia. *Thermoelectric materials*. en. Page Version ID: 989933448. Nov. 2020. URL: [https://en.wikipedia.org/w/index.php?title=Thermoelectric\\_materials&oldid=989933448](https://en.wikipedia.org/w/index.php?title=Thermoelectric_materials&oldid=989933448) (visited on 22/11/2020).
- [3] Eddwi H. Hasdeo et al. 'Optimal band gap for improved thermoelectric performance of two-dimensional Dirac materials'. In: *Journal of Applied Physics* 126.3 (July 2019), p. 035109. ISSN: 1089-7550. DOI: 10.1063/1.5100985. URL: <http://dx.doi.org/10.1063/1.5100985>.
- [4] G. Jeffrey Snyder and Eric S Toberer. 'Complex thermoelectric materials'. eng. In: *Nature materials* 7.2 (2008), pp. 105–114. ISSN: 1476-1122.
- [5] Jorge Osvaldo Sofo and GD Mahan. 'Optimum band gap of a thermoelectric material'. In: *Physical Review B* 49.7 (1994), p. 4565.
- [6] Tsai. Ming-Hung and Yeh. Jien-Wei. 'High-Entropy Alloys: A Critical Review'. In: *Materials Research Letters* 2.3 (2014), pp. 107–123. DOI: 10.1080/21663831.2014.912690. eprint: <https://doi.org/10.1080/21663831.2014.912690>. URL: <https://doi.org/10.1080/21663831.2014.912690>.
- [7] Joshua Gild et al. 'A high-entropy silicide: (Mo<sub>0.2</sub>Nb<sub>0.2</sub>Ta<sub>0.2</sub>Ti<sub>0.2</sub>W<sub>0.2</sub>)Si<sub>2</sub>'. In: *Journal of Materiomics* 5.3 (2019), pp. 337–343. ISSN: 2352-8478. DOI: <https://doi.org/10.1016/j.jmat.2019.03.002>. URL: <https://www.sciencedirect.com/science/article/pii/S2352847819300334>.
- [8] Mari Mathillas Røsvik. *Structural Characterization of High Entropy Metal Silicide Alloys*. 2021.
- [9] Burkov. A. 'Silicide Thermoelectrics: Materials for Energy Harvesting'. In: *physica status solidi (a)* 215 (June 2018). DOI: 10.1002/pssa.201800105.
- [10] S. J. Clark et al. 'Structure and electronic properties of FeSi<sub>2</sub>'. In: *Phys. Rev. B* 58 (16 Oct. 1998), pp. 10389–10393. DOI: 10.1103/PhysRevB.58.10389. URL: <https://link.aps.org/doi/10.1103/PhysRevB.58.10389>.

- [11] Voicu Popescu and Alex Zunger. ‘Effective Band Structure of Random Alloys’. In: *Phys. Rev. Lett.* 104 (23 June 2010), p. 236403. DOI: 10.1103/PhysRevLett.104.236403. URL: <https://link.aps.org/doi/10.1103/PhysRevLett.104.236403>.
- [12] H Lange. ‘Electronic properties of semiconducting silicides’. In: *physica status solidi (b)* 201.1 (1997), pp. 3–65.
- [13] R. Eppenga. ‘Ab initio band-structure calculation of the semiconductor  $\beta$ -FeSi<sub>2</sub>’. In: *Journal of Applied Physics* 68.6 (1990), pp. 3027–3029. DOI: 10.1063/1.346415. eprint: <https://doi.org/10.1063/1.346415>. URL: <https://doi.org/10.1063/1.346415>.
- [14] ISMEAR - *Vaspwiki*. URL: <https://www.vasp.at/wiki/index.php/ISMEAR>.
- [15] Xingxing Li and Jinlong Yang. ‘First-principles design of spintronics materials’. In: *National Science Review* 3.3 (Apr. 2016), pp. 365–381. ISSN: 2095-5138. DOI: 10.1093/nsr/nww026. eprint: <https://academic.oup.com/nsr/article-pdf/3/3/365/31566317/nww026.pdf>. URL: <https://doi.org/10.1093/nsr/nww026>.